Article

Achieving Ultra-Low-Sulfur Model Diesel Through Defective *Keggin*-Type Heteropolyoxometalate Catalysts

Natali de la Fuente [1], Jin An Wang [1,*], Lifang Chen [1,2], Miguel A. Valenzuela [1], Luis E. Noreña [2], Elizabeth Rojas [2], Julio González [3], Mu He [4], Jiang Peng [4] and Xiaolong Zhou [4]

[1] Escuela Superior de Ingeniería Química e Industrias Extractivas, Instituto Politécnico Nacional, Col. Zacatenco, Ciudad de México 07738, Mexico; ndelafuente@ipn.mx (N.d.l.F.); lchen@ipn.mx (L.C.); mavalenz@ipn.mx (M.A.V.)

[2] Departamento de Ciencias Básicas, Universidad Autónoma Metropolitana-Azcapotzalco, Av. San Pablo 180, Col. Reynosa Tamaulipas, Ciudad de México 02200, Mexico; lnf@azc.uam.mx (L.E.N.); elithroga@gmail.com (E.R.)

[3] TecNM-Tecnológico de Estudios Superiores de Coacalco, 16 de Septiembre 54, Col. Cabecera Municipal, Estado de México 55700, Mexico; jgon88@hotmail.com

[4] International Joint Research Center of Green Chemical Engineering, East China University of Science and Technology, Shanghai 200237, China; muhe9702@163.com (M.H.); y12203007@mail.ecust.edu.cn (J.P.); xiaolong@ecust.edu.cn (X.Z.)

* Correspondence: jwang@ipn.mx; Tel.: +52-55-57296000 (ext. 54276)

Abstract: Various *Keggin*-type heteropolyoxometalate catalysts with structural defects and surface acidity were synthesized by immobilizing 12-phosphotungstic acid (HPW) on mesoporous SBA−15, to produce near-zero-sulfur diesel fuel. As the calcination temperature increased, the W=O and the corner-shared W–O–W bonds in the *Keggin* unit partially broke, creating oxygen defects, as evidenced by the Rietveld refinement and in situ FTIR characterization. All the catalysts contained Lewis (L) and Brønsted (B) acid sites, with L acidity predominant. The relative intensity of the IR band (I_{980}) of W=O bond inversely correlated with the number of L acid sites as the calcination temperature varied, suggesting that oxygen defects contributed to the Lewis acid sites formation. In the oxidation of dibenzothiophene (DBT) in a model diesel within a biphasic system, DBT conversion exceeded 99% under the optimal reaction conditions (reaction temperature 70 °C, reaction time 60 min, H_2O_2/sulfur molar ratio 8, H_2O_2/formic acid molar ratio 1.5, catalyst concentration 2 mg/mL). The influence of fuel composition and addition of indole and 4,6-DMDBT on DBT oxidation were also evaluated. Indole and cyclohexene negatively impacted the DBT oxidative removal. Oxygen defects served as active centers for competitive adsorption of sulfur compound and oxidant. Both L and B acid sites were involved in transferring O atom from peroxophosphotungstate complex to sulfur in DBT, resulting in $DBTO_2$ sulfone, which was immediately extracted by polar acetonitrile. This study confirms that structural defects and surface acidity are crucial in the deep oxidative desulfurization (ODS) reaction, and in enabling the simultaneous oxidation and separation of refractory organosulfur compounds in a highly efficient model diesel.

Keywords: near-zero-sulfur diesel; dibenzothiopene; deep oxidative desulfurization; oxygen defects; heteropolyoxometalate

1. Introduction

A broad spectrum of organosulfur compounds, including mercaptans, sulfides, thiophenes, benzothiophene (BT), dibenzothiophene (DBT), and its derivatives in fossil fuels, are a significant source of sulfur-related air pollution [1,2]. These hazardous sulfur compounds must be eliminated before fuel combustion to meet the increasingly strict requirements of the new environmental regulations. Hydrodesulfurization (HDS) is a commonly used technique to remove these sulfur compounds from crude oil before it is

fed into the fluid catalytic cracking (FCC) unit [2–4]. However, HDS is a nonselective hydrogenation process that operates under moderate reaction temperatures (300–500 °C) and high pressures (50–130 atm) and requires expensive hydrogen consumption. Furthermore, HDS is not very effective for the deep removal of refractory sulfur compounds such as polyaromatic DBT and its methyl-substituted derivatives like 4,6-dimethyl dibenzothiophene (4,6-DMDBT) due to their steric hindrance and high resistance to hydrodesulfurization. This is evidenced by the considerable concentration of such compounds in hydrotreated fuels [5]. Economically, the HDS technique efficiently reduces sulfur concentration from a low weight percentage to approximately hundreds of ppm at a reasonable cost. To further reduce the sulfur concentration from a hundred ppm to an ultralow (<10 ppm) or near-zero concentration, the HDS operation parameters must be modified by elevating the reaction temperature and pressure and by increasing the H_2/oil ratio and catalyst volume [6]. These modifications undoubtedly increase the total operation cost, and harsh reaction conditions may shorten the catalyst's lifetime.

Alternative desulfurization techniques, such as biodesulfurization [7–9], extractive/adsorptive desulfurization [10,11], and oxidative desulfurization [12–14], have been explored. Oxidative desulfurization (ODS) has several advantages over the HDS technique, including milder reaction conditions (low reaction temperature and ambient pressure), high selectivity for removal of sterically hindered aromatic sulfur compounds, and no need for expensive hydrogen consumption [13,14]. Generally, ODS consists of two steps: oxidation of aromatic sulfurs to the corresponding polar sulfones, and the removal of the oxidized compounds through extraction and adsorption. Various oxidants have been used for sulfur oxidation, including hydrogen peroxide [15], molecular oxygen [16], tert-butylhydroperoxide [17], and solid oxidizing agent [18]. While molecular oxygen or air is the most economical oxidant for ODS, it requires a high reaction temperature for the sulfur oxidation reactions, and usually, the sulfur removal efficiency is relatively low. Eseva and coworkers have reported the ODS results of dibenzothiophene using catalysts containing an Anderson-type polyoxometalate. The CoMo/IL−SBA−15 catalyst synthesized using functional-group-grafted mesoporous support material showed the best catalytic activity and stability. Utilization of hot air as oxidant is attractive. However, the reaction temperature had to be increased to 120 °C [19]. Hydrogen peroxide (H_2O_2) is widely used in ODS due to its high content of oxygen (47% oxygen), strong oxidation power, and environmentally friendly nature. After ODS treatment, the polar products (sulfones) can be separated by extraction from fuel using a non-miscible solvent, with acetonitrile commonly used as a polar solvent in the ODS process. Although the use of oxidant and polar extracting agent may increase the operation cost, the total cost of the ODS process is approximately 15–20% lower than that of HDS for the same scale [20].

In the catalytic ODS process, an active catalyst is essential. The Lewis acidity of transition metal oxide catalysts takes the decisive role in the sulfur oxidation. For example, the 4,6-DMDBT conversion was reported to be almost proportional to the number of Lewis acid sites in the MoO_3/SBA−15 catalysts [21]. A similar relationship was also established for the V_2O_5/Zr-SBA−15 [22] and mesoporous titania–silica–polyoxometalate nanocomposite [23]. In these catalysts, oxygen defects correlate with the Lewis acid sites and catalytic activities. Some other researchers have claimed that catalytic efficiency in oxidative desulfurization is enhanced by B acid sites coupled with a small number of L acid sites [24].

Heteropolyacids, such as phosphotungstic acid ($H_3PW_{12}O_{40}$) and phosphomolybdic acid ($H_3PMo_{12}O_{40}$), dispersed on various solids, have been reported for ODS reactions [25–28]. It is well known that 12-phosphotungstic acid is the strongest solid acid among the heteropolyacid family, and it is often used as catalyst for acid−catalyzed reactions due to its high redox properties, tunable acidity, hydrolytic stability, and defective *Keggin* structure. $H_3PW_{12}O_{40}$/SiO_2 and $H_3PW_{12}O_{40}$/TiO_2 catalysts contain strong Brønsted acidity and are active in the ODS of fuels [29,30]. Novel homogeneous catalysts, such as aqueous $H_8PV_5Mo_7O_{40}$, were also applied for the oil ODS process under conditions of 120 °C temperature, 20 bar oxygen pres-

sure, and 6 h reaction time with a volume water/oil ratio of 10 [31]. However, homogeneous catalysts face difficulties of reuse and separation. Complete reviews of the heteropolyacid family in the ODS reactions can be found in reference [24]. In the literature, the roles of structural defects in *Keggin* structure and the B and L acid sites in the ODS reactions are not clear yet and are rarely reported.

In the current work, we aim to design a novel catalyst for near-zero-sulfur fuel production by simultaneously oxidizing and separating DBT in a biphasic system consisting of a polar solvent (acetonitrile) and a nonpolar phase (n-hexadecane) containing 300 ppm DBT. We applied a series of defective heteropolyoxometalate catalysts by immobilizing phosphotungstic acid (HPW) on SBA−15. The crystalline structure, textural properties, morphological features, W oxidation state, and chemical valence of the catalysts were characterized by a variety of techniques including X-ray diffraction (XRD), N_2 adsorption–desorption isotherms, transmission electron microscopy (TEM), X−ray photoelectronic spectroscopy (XPS), and in situ FTIR of pyridine adsorption. In situ, FTIR characterization monitored the thermal stability and oxygen defects in the *Keggin* unit of the dispersed phosphotungstic acid. Structural defect concentrations calcined at different temperatures were determined by the Rietveld refinement method. Particular attention was paid to the possible correlation of structural defects and surface acidity with the catalytic activity to provide new insight into the ODS reaction mechanism.

2. Results and Discussion

2.1. XRD Analysis and Rietveld Refinement

The XRD patterns of five catalysts (HPW/SBA−15) with different 12-phosphotungstic acid (HPW) content calcined at 100, 200, and 400 °C are presented in Figure 1. For the catalysts calcined at 100 °C, Figure 1A shows one broad peak between 15 and 35°, which corresponds to the amorphous silica SBA−15. With an HPW content 10 wt%, two very weak peaks at 26.21 and 27.65° appear, corresponding to the reflection of (222) and (400) planes of tungstophosphoric acid crystals. This indicates a small crystallite size and high dispersion of the heteropolyacid nanoparticles. As the HPW content increases to 20 and 30 wt%, additional peaks emerge at two-theta angles of 10.5°, 14.5°, 17.5°, 20.4°, 22.5°, 26.2°, 29.0°, 35.8°, 37.4°, 41.4°, 46.40°, 54.0°, 59.8°, and 62.10°, corresponding to the reflections of different planes with Miller index (110), (200), (211), (220), (310), (222), (400), (420), (510), (611), (550), (650), and (660), respectively, in the tungstophosphoric acid crystals [32,33]. The peak at 8.49° indicates the existence of water molecules in the crystals. These XRD peaks collectively confirm the crystalline structure of hydrated tungstophosphoric acid with *Keggin* units.
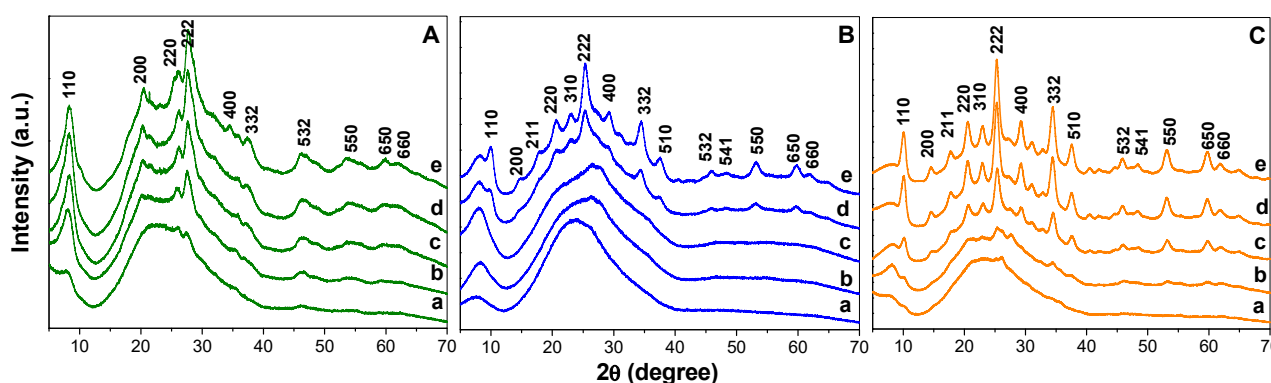
Figure 1. XRD patterns of HPW/SBA−15 catalysts calcined at different temperatures (**A**) 100 °C, (**B**) 200 °C and (**C**) 400 °C. (a): 10 wt% $H_3PW_{12}O_{40}$/SBA−15; (b): 20 wt% $H_3PW_{12}O_{40}$/SBA−15; (c): 30 wt% $H_3PW_{12}O_{40}$/SBA−15; (d): 40 wt% $H_3PW_{12}O_{40}$/SBA−15; (e): 50 wt% $H_3PW_{12}O_{40}$/SBA−15.

For the samples calcined at 200 °C, Figure 1B shows a strong reduction in the intensity of the peak at 8.49°, signifying the desorption of water from the heteropolyacid crystalline structure. In samples with an HPW content lower than 30 wt%, only very weak peaks appeared between 28° and 35°, with no other diffraction peaks corresponding to the crystalline phase of HPW. This suggests that after losing most of the crystal water molecules at 200 °C, tungstophosphoric acid crystals have crystallite size smaller than 4 nm, which is the lowest detectable limit of the X-ray diffractometer. These nanosized crystals are highly dispersed on the surface of the mesoporous support. This observation may also suggest that water molecules functioned as linkers for the *Keggin* units, facilitating the formation of larger crystals. The removal of these water linkers from the heteropolyacid structure resulted in the crystals breaking into smaller sizes.

Upon calcination at 400 °C, Figure 1C shows a further reduction in the intensity of the peak at 8.49°, indicating additional desorption of crystal water from the solid. The XRD peaks corresponding to the planes of dehydrated heteropolyacid crystals exhibit sharper reflections for samples with 40 and 50 wt% HPW, suggesting an increase in crystallite size. Although structural defects were introduced at a calcination temperature of 400 °C, the *Keggin* structure remained intact. The Rietveld refinement method was employed to determine the structural defects in the heteropolyacid crystals. Figure 2 presents a Rietveld plot for the 40 wt% HPW/SBA−15 sample calcined at 400 °C. The structural data, including space group, symmetry, phase composition, lattice cell parameters, crystallite size, and oxygen defects obtained from the Rietveld refinement, are summarized in Table 1.
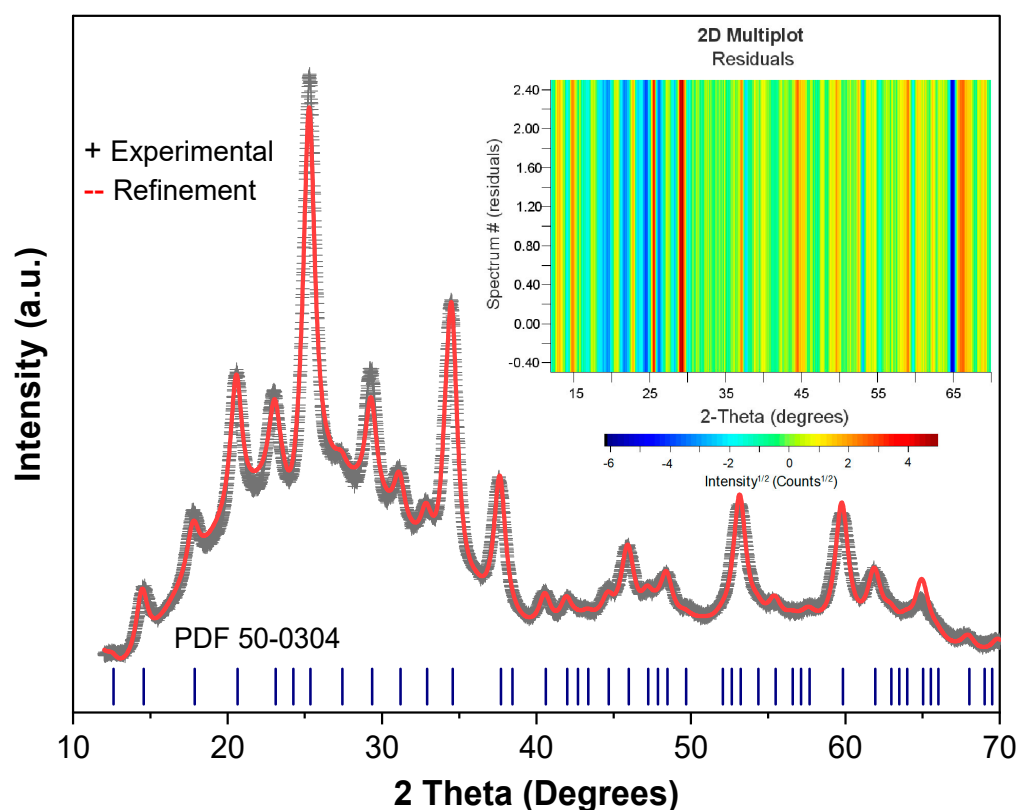
Figure 2. Rietveld refinement plot of the 50 wt% HPW/SBA−15 calcined at 400 °C. The black crosses correspond to experimental data, and the red solid line corresponds to theorical data. The blue marks correspond to crystalline structure of monoclinic $H_3PW_{12}O_{40}$. The inset 2D multiplot indicates the residual between the experimental and the calculated data. $R_{wp} = 1.95\%$.

Table 1. The structural data obtained from the Rietveld refinement *.

Sample	Phase	Space Group	Symmetry	Crystallite Size (nm)	Lattice Cell Parameters (Å) a	b	c	Oxygen Defects (%)	R_{wp} (%)
10A	$H_3PW_{12}O_{40} \cdot 21H_2O$	Pcca	Orthorhombic	15.5	21.041	13.286	18.880	ND	1.45
	$H_3PW_{12}O_{40}$	Pn-3m	Cubic	4.7	11.860			ND	
10B	$H_3PW_{12}O_{40}$	Pn-3m	Cubic	11.7	11.772			0.10	1.40
10C	$H_3PW_{12}O_{40}$	Pn-3 m	Cubic	6.8	11.722			ND	1.12
20A	$H_3PW_{12}O_{40} \cdot 21H_2O$	Pcca	Orthorhombic	14.4	21.040	13.286	18.879	ND	2.13
	$H_3PW_{12}O_{40}$	Pn-3m	Cubic	5.4	11.874			ND	
20B	$H_3PW_{12}O_{40}$	Pn-3m	Cubic	6.6	12.141			0.1	2.31
20C	$H_3PW_{12}O_{40}$	Pn-3m	Cubic	6.8	11.797			14.7	2.57
30A	$H_3PW_{12}O_{40} \cdot 21H_2O$	Pcca	Orthorhombic	14.4	20.788	13.086	18.876	ND	2.36
	$H_3PW_{12}O_{40}$	Pn-3m	Cubic	7.1	11.777			ND	
30B	$H_3PW_{12}O_{40}$	Pn-3m	Cubic	12.2	12.160			5.90	2.51
30C	$H_3PW_{12}O_{40}$	Pn-3m	Cubic	6.9	11.730			22.40	1.28
40A	$H_3PW_{12}O_{40} \cdot 21H_2O$	Pcca	Orthorhombic	17.8	20.788	13.086	18.879	ND	1.26
	$H_3PW_{12}O_{40}$	Pn-3m	Cubic	6.0	12.191			ND	
40B	$H_3PW_{12}O_{40}$	Pn-3m	Cubic	12.2	12.183			9.10	3.69
40C	$H_3PW_{12}O_{40}$	Pn-3m	Cubic	9.3	12.183			20.50	1.42
50A	$H_3PW_{12}O_{40} \cdot 21H_2O$	Pcca	Orthorhombic	10.2	20.789	13.190	19.332	ND	3.36
	$H_3PW_{12}O_{40}$	Pn-3m	Cubic	5.1	12.101			37.31	3.52
50B	$H_3PW_{12}O_{40}$	Pn-3m	Cubic	12.3	12.181			34.70	4.45
50C	$H_3PW_{12}O_{40}$	Pn-3m	Cubic	9.4	12.173			28.10	1.95

* The numbers 10, 20, 30, 40, and 50 indicate the heteropolyacid content (wt%); the letters A, B, and C correspond to the sample calcination temperature 100, 200, and 400 °C, respectively. For example, 10A: 10 wt% $H_3PW_{12}O_{40}$/SBA−15 calcined at 100 °C; 10B: 10 wt% $H_3PW_{12}O_{40}$/SBA−15 calcined at 200 °C, and 10C: 10 wt% $H_3PW_{12}O_{40}$/SBA−15 calcined at 400 °C. R_{wp}: weighted-profile R factors (%). Usually, an R value smaller than 10% indicates good structure simulation. ND: not determined.

As shown in Table 1, the 12−phosphotungstic acid dispersed on the catalysts and calcined at 100 °C contained two phases, cubic and orthorhombic, with the orthorhombic phase containing water molecules. After calcination at 200 °C, only the cubic phase remained, signifying a phase transformation from orthorhombic to cubic due to the loss of water. This transformation was accompanied by a change in crystallite size as a result of dehydration and partial decomposition of the *Keggin* unit. Consequently, oxygen defects emerged in the crystalline structure, the concentration of which varied with both the calcination temperature and the content of heteropolyacid. Higher loading of heteropolyacid and increased calcination temperature led to a greater number of oxygen defects.

2.2. Textural Properties of $H_3PW_{12}O_{40}$/SBA−15

Figure 3 shows the hysteresis loops of N_2 adsorption–desorption isotherms and the pore diameter distributions of the catalysts. Textural data including surface area, average pore size, and pore volume of SBA−15 and HPW/SBA−15 catalysts are summarized in Table 2. As seen in Figure 3A, all catalysts displayed type IV isotherms with H1 hysteresis loops, indicative of mesoporous materials with cylindrical pore channels, consistent with the classification of the International Union of Pure and Applied Chemistry (IUPAC) [34]. The pore size, derived from the BJH model applied to the N_2 desorption branch data, ranged from 6.0 to 8.0 nm, with a maximum of 7.6 nm. The Brunauer–Emmett–Teller (BET) surface areas varied between 640 and 440 m^2/g, influenced by the heteropolyacid content (Figure 3B). A higher HPW loading corresponded to a reduced surface area. The pore volume diminished from 1.16 cm^3/g to 0.65 cm^3/g as the HPW content increased from 10 to 50 wt%, attributed to the partial obstruction of the mesopores by HPW nanoparticles. Notably, the shapes of the N_2 adsorption–desorption isotherms and the pore diameter distribution profiles were consistent across all catalysts.
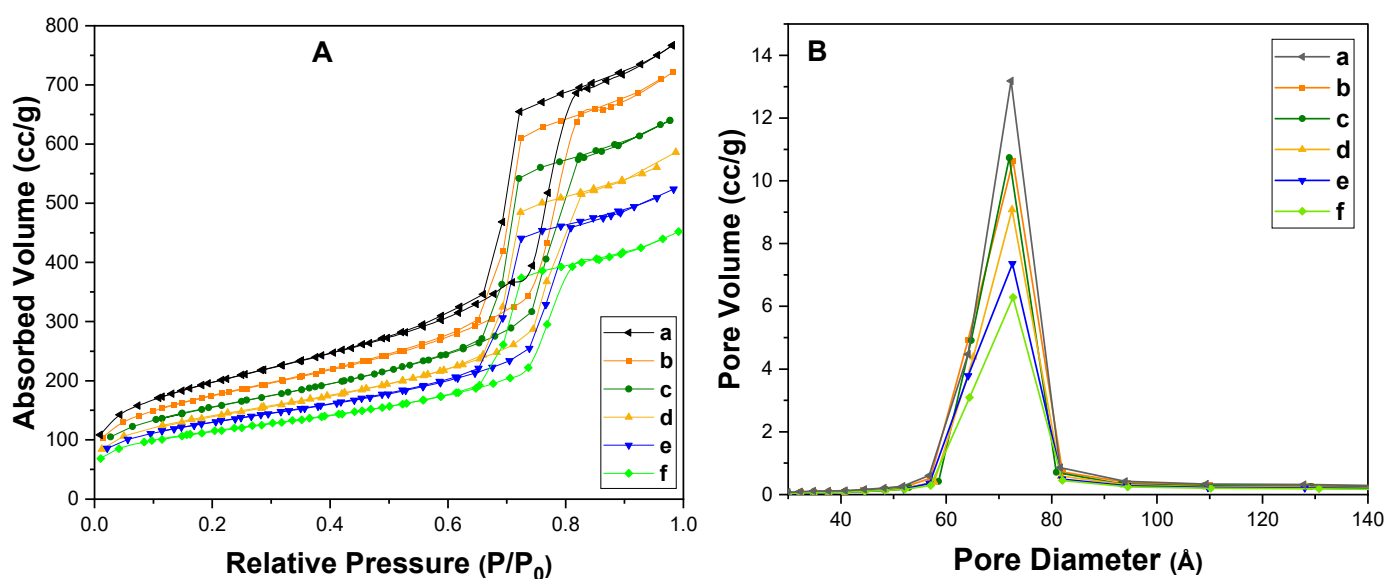
Figure 3. N_2 adsorption–desorption isotherms loops (**A**) and pore size distribution profiles (**B**) of the HPW/SBA−15 catalysts. (a): SBA−15; (b): 10 wt% $H_3PW_{12}O_{40}$/SBA−15; (c): 20 wt% $H_3PW_{12}O_{40}$/SBA−15; (d): 30 wt% $H_3PW_{12}O_{40}$/SBA−15; (e): 40 wt% $H_3PW_{12}O_{40}$/SBA−15; (f): 50 wt% $H_3PW_{12}O_{40}$/SBA−15.

Table 2. Textural properties, elements of P and W nominal content, and W/S molar ratio in the ODS reaction.

Catalysts	Surface Area (m^2/g)	Average Pore Size (nm)	Pore Volume (cm^3/g)	P (mmol)	W (mmol)	W/S Ratio *
SBA−15	715	6.5	1.15	0	0	0
10 wt%HPW/SBA−15	629	7.17	1.07	0.00069	0.0083	0.59
20 wt%HPW/SBA−15	563	7.22	0.90	0.00139	0.0167	1.18
30 wt%HPW/SBA−15	503	7.11	0.86	0.00208	0.0252	1.77
40 wt%HPW/SBA−15	464	7.21	0.81	0.00278	0.0333	2.36
50 wt%HPW/SBA−15	411	7.15	0.78	0.00347	0.0416	2.94

* W/S values were calculated from 20 mg catalyst sample and 10 mL of 300 ppm DBT in n-hexadecane.

2.3. Morphological Features

The morphological characteristics of SBA−15 and HPW/SBA−15 samples were examined using transmission electron microscopy (TEM, JEM-ARM200 CF, JEOL Ltd., Tokyo, Japan). The SBA−15 support exhibited a well-ordered hexagonal mesoporous structure (Figure 4A), with a pore diameter of approximately 7.5 nm and a pore wall thickness of about 2–3 nm. After impregnation with heteropolyacid, the mesoporous structure of SBA−15 remained largely intact, indicating minimal disruption to the support structure. The heteropolyacid was well-dispersed across the surface of the SBA−15 solid (Figure 4B,C). Additionally, some small particles with a diameter of around 5 nm were observed, some of which were located within the pores. The majority of the HPW particles were aligned along the pore channels (Figure 4D). The energy-dispersive X-ray spectroscopy (EDS) spectrum from a selected area in the TEM micrograph (Figure 4E) revealed the presence of oxygen (O), phosphorus (P), and tungsten (W), confirming that these particles corresponded to $H_3PW_{12}O_{40}$ crystals, which were too small to be detected by XRD analysis. Figure 4F displays a WL profile obtained from Figure 4D along the marked path, further validating the distribution of tungsten (W) in $H_3PW_{12}O_{40}$ on the SBA−15 surface.
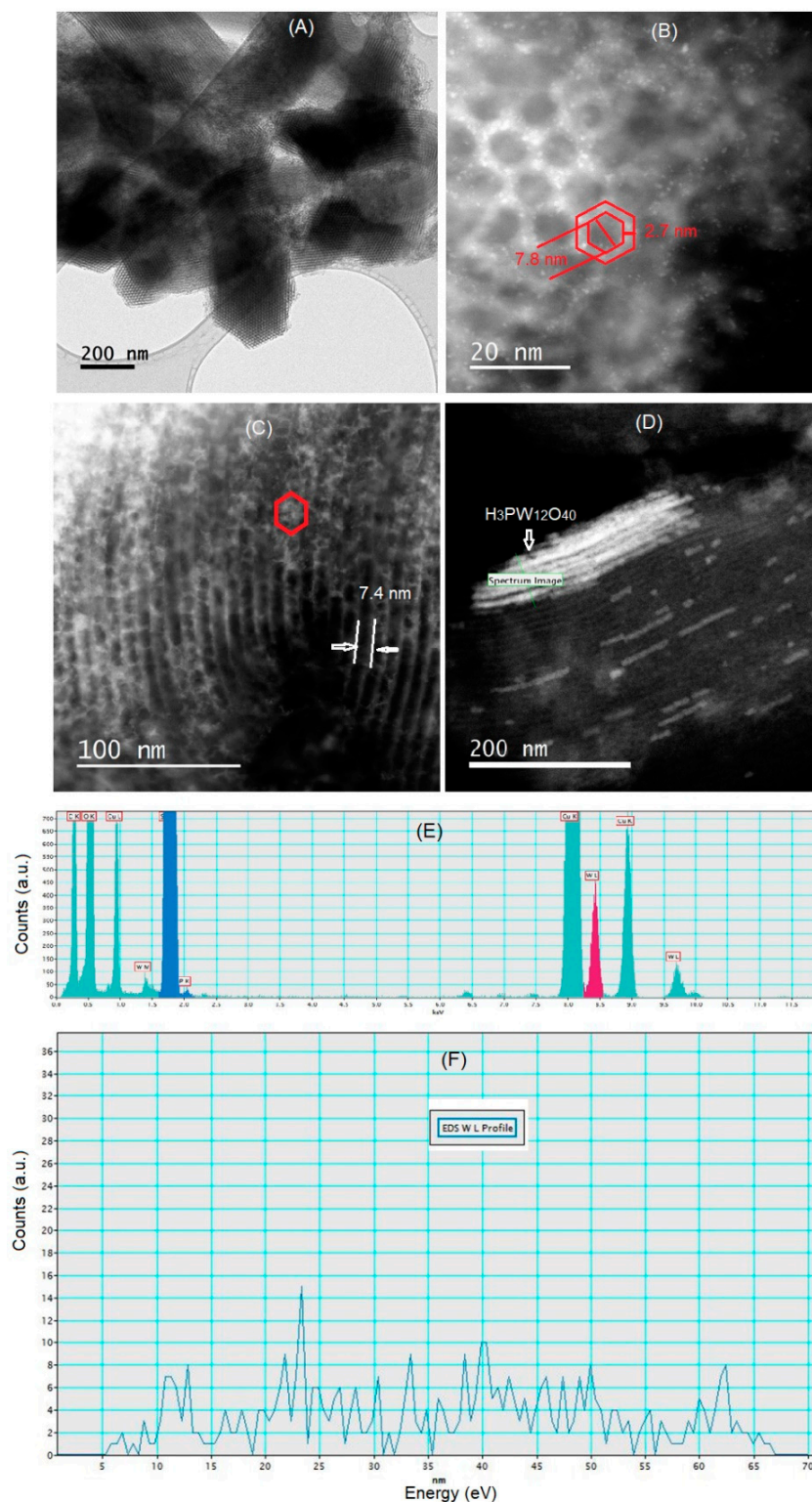
Figure 4. TEM micrographs and EDS spectra of SBA−15 and $H_3PW_{12}O_{40}$/SBA−15 calcined at 200 °C. (**A**) SBA−15 support; (**B**) 20 wt% $H_3PW_{12}O_{40}$/SBA−15 calcined at 200 °C; (**C**) 30 wt% $H_3PW_{12}O_{40}$/SBA−15 calcined at 200 °C; (**D**) 40 wt% $H_3PW_{12}O_{40}$/SBA−15 calcined at 200 °C; (**E**) EDS profile of the selected area in (**C**); (**F**) EDS profile of the selected area in (**D**).

2.4. In Situ FTIR Characterization

The dispersed *Keggin* units of the $H_3PW_{12}O_{40}$/SBA−15 catalysts contain a variety of surface species, including adsorbed water, hydroxyl groups, and various tungsten–oxygen

bonds (W=O_t, W–O–W, and W–O–P). In situ, FTIR characterization was performed to assess their thermal stability and changes with temperature. Figure 5 presents five sets of in situ FTIR spectra recorded at temperatures ranging from 50 to 450 °C. Across all catalysts, a band at 1640 cm^{-1} was observed, attributed to the stretching vibration of OH species in surface-adsorbed water. The intensity of this band diminished and vanished by 200 °C, signifying the desorption of surface-adsorbed water. At 100 °C, all samples exhibited characteristic IR bands of the *Keggin* structure of $[PW_{12}O_{40}]^{3-}$, present at 1080, 980, 893, and 803 cm^{-1}, respectively [35–37]. The band at 1080 cm^{-1} is indicative of the P–O stretching vibration in the central PO_4 unit, while the 980 cm^{-1} band corresponds to the stretching vibration of the terminal W=O_t bond. The bands at 893 and 803 cm^{-1} are associated with the stretching motions of two types of W–O–W bridged bonds: the W–Oc–W stretching mode (inter-bridges between corner-sharing octahedra) at 893 cm^{-1} and the W–Oe–W stretching mode (intra-bridges between edge-sharing octahedra) at 822 cm^{-1} [37–40]. These findings confirm the intact *Keggin* structure post-dispersion on SBA−15, showcasing chemical stability at 100 °C.
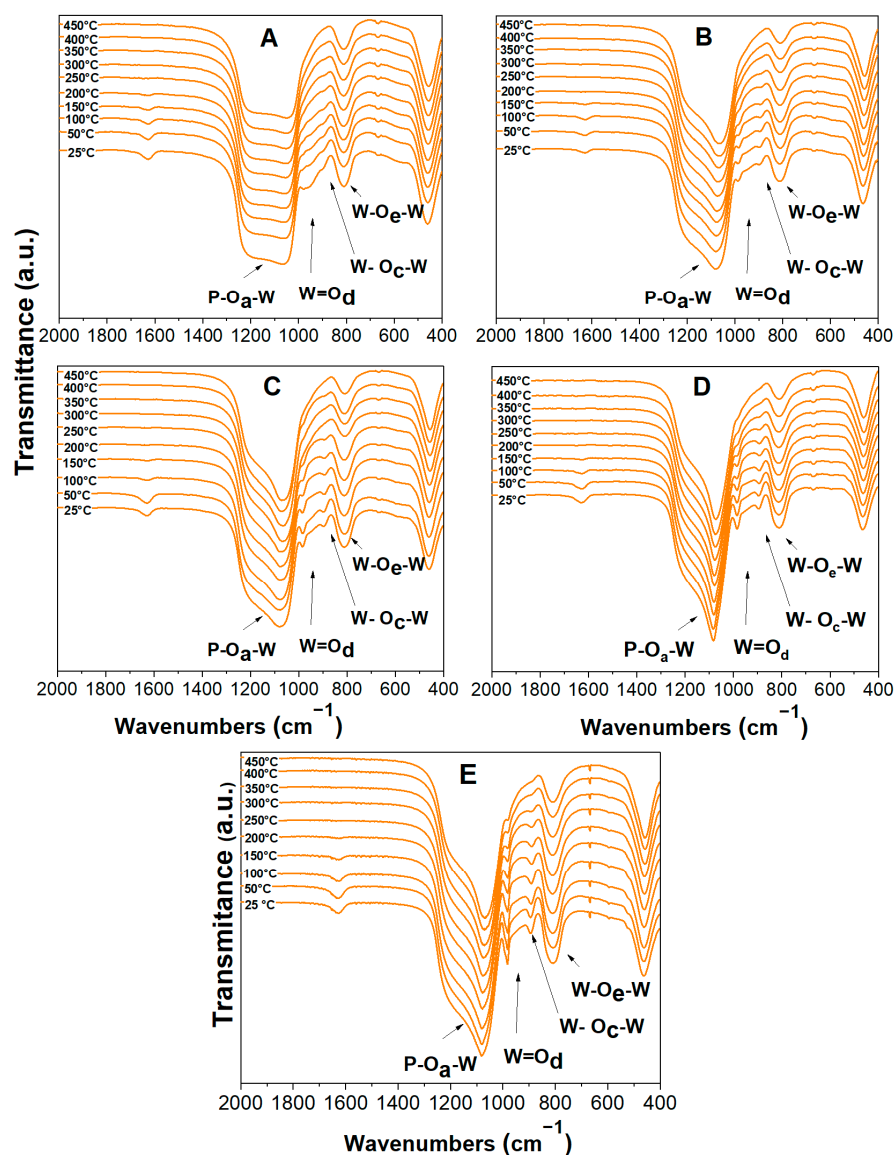
Figure 5. In situ FTIR spectra of catalysts at different temperatures. (**A**) 10 wt% $H_3PW_{12}O_{40}$/SBA−15; (**B**) 20 wt% $H_3PW_{12}O_{40}$/SBA−15; (**C**) 30 wt% $H_3PW_{12}O_{40}$/SBA−15; (**D**) 40 wt% $H_3PW_{12}O_{40}$/SBA−15; (**E**) 50 wt% $H_3PW_{12}O_{40}$/SBA−15.

With the temperature increase to 200 °C, a decline in the intensity of the terminal W=O_t double bond was observed, and it completely disappeared by 300 °C, indicating the creation of oxygen defects. Similarly, the W–Oc–W stretching mode diminished after thermal treatment above 300 °C. Notably, a broad band at 1200–1000 cm^{-1} appeared, corresponding to the asymmetric stretching of the Si–O–Si bond in SBA−15 silica. This band partially overlaps with the W–O–P stretching vibration, though the latter remains distinct and sharper. The bands around 809 and 455 cm^{-1} were assigned to the stretching and bending vibrations of Si–O–Si in the SBA−15 framework [38,39], causing overlap with the W–Oe–W band at 803 cm^{-1}.

Catalysts with higher HPW content (40 and 50 wt%) displayed more excellent thermal stability, maintaining their *Keggin* fingerprint IR bands even at 400 °C. In contrast, catalysts with lower HPW content exhibited higher dispersion and stronger interaction with the SBA−15 support, leading to more pronounced deformation of the *Keggin* unit. This interaction resulted in easier cleavage of W=O_t and W–O_c–W bonds and removal of oxygen species at elevated temperatures. The v_{as}(W–O_c–W) mode is susceptible to hydration effects due to hydrogen bonding, weakening W–O bond strength and forming a lacunary heteropoly anion with a defective *Keggin* unit. This behavior is evidenced by the concurrent disappearance of the band at 1620 cm^{-1}, correlating with the degree of dehydration. Overall, the in situ FTIR characterization suggests that oxygen defects in the *Keggin* structure emerge at around 200 °C. While the *Keggin* framework withstands up to 400 °C with an increase in structural defects, it undergoes thermal decomposition into WO_3 above 600 °C [40].

2.5. Surface Acidity

Figure 6 displays the in situ FTIR spectra of pyridine adsorption on the catalysts, demonstrating the presence of both Lewis (L) and Brønsted (B) acid sites across all samples. The Lewis acid sites are characterized by IR absorption bands at 1445, 1579, and 1594 cm^{-1}, while the Brønsted acid sites are identified by bands at 1542 and 1687 cm^{-1} [41–43]. Additionally, a band observed at approximately 1489 cm^{-1} corresponds to the pyridine molecule's vibration associated with both L and B acid sites. The concentrations of these acid sites, as analyzed in Table 3, show that Lewis acidity predominates on the catalyst surfaces. As the HPW content increases from 10 to 30 wt%, there is a corresponding rise in both L and B acid site concentrations. However, this trend reverses with further increases in HPW content, leading to a decrease in acid site concentrations in samples with 40 and 50 wt% HPW.
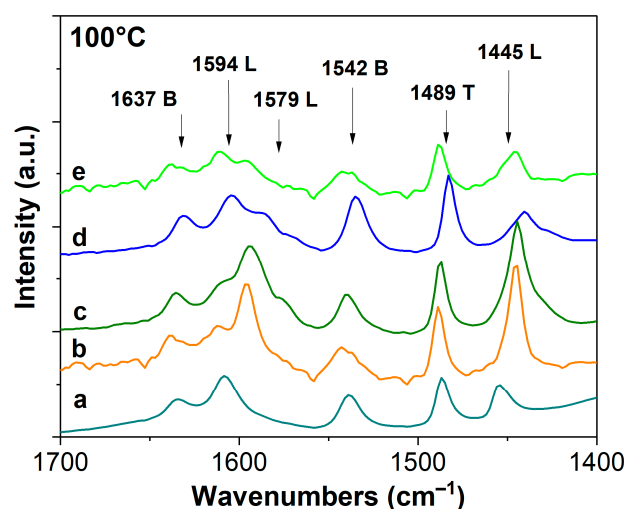
Figure 6. In situ FTIR spectra of pyridine adsorption on the catalysts. (a) 10 wt% $H_3PW_{12}O_{40}$/SBA−15; (b) 20 wt% $H_3PW_{12}O_{40}$/SBA−15; (c) 30 wt% $H_3PW_{12}O_{40}$/SBA−15; (d) 40 wt% $H_3PW_{12}O_{40}$/SBA−15; (e) 50 wt% $H_3PW_{12}O_{40}$/SBA−15.

Table 3. Surface acidity data of the different catalysts calcined at different temperatures and obtained from the FTIR spectra of pyridine adsorption recorded at 100 °C in IR cell.

Catalysts	Calcination Temp. (°C)	Lewis Acidity (µmol/g)	Brønsted Acidity (µmol/g)	Total Acidity (µmol/g)
10 wt%HPW/SBA−15	100	687	56	743
20 wt%HPW/SBA−15	100	730	76	806
30 wt%HPW/SBA−15	100	823	162	985
40 wt%HPW/SBA−15	100	496	46	542
50 wt%HPW/SBA−15	100	389	28	417
10 wt%HPW/SBA−15	200	894	62	956
20 wt%HPW/SBA−15	200	1216	160	1376
30 wt%HPW/SBA−15	200	1207	367	1574
40 wt%HPW/SBA−15	200	1055	267	1322
50 wt%HPW/SBA−15	200	861	133	994
10 wt%HPW/SBA−15	400	933	80	1013
20 wt%HPW/SBA−15	400	1277	135	1412
30 wt%HPW/SBA−15	400	1280	238	1518
40 wt%HPW/SBA−15	400	826	113	939
50 wt%HPW/SBA−15	400	737	139	876

The molar ratio of B/L sites, which is indicative of the relative prevalence of Brønsted over Lewis acidity, varies with the tungstophosphoric acid content and the calcination temperature. Specifically, at 100 °C, the B/L ratio increases from 0.082 to 0.092 and 0.197 as the HPW content rises from 10 wt% to 20 and 30 wt%, respectively. Beyond 30 wt% HPW, this ratio decreases. A similar trend is observed in samples calcined at 200 and 400 °C. The samples containing 20 and 30 wt% HPW consistently exhibit the highest surface acidity and the most significant B/L ratios, highlighting their enhanced catalytic potential.

2.6. XPS Analysis

Figure 7 shows the survey XPS spectra for the samples calcined at 100, 200, and 400 °C, revealing peaks corresponding to the elements O, P, W, and Si. The signal for phosphorus (P) is notably weak, likely due to its central position within the *Keggin* structure, which reduces its surface exposure. Figure 8 provides the deconvolution of the O1s and W 4f core-level spectra. The broad O1s peaks observed in the $H_3PW_{12}O_{40}$/SBA−15 samples, calcined at different temperatures, are indicative of the various oxygen environments in the material. The symmetry in the O1s core-level peaks is attributed to the fully symmetrical *Keggin* unit. Upon deconvolution, the O1s spectra reveal four distinct components with binding energies at 531.4, 532.4, 533.5, and 534.7 eV. These correspond to oxygen atoms in W–O–P, W–O–W, and W=O bonds, and adsorbed water, respectively [44].
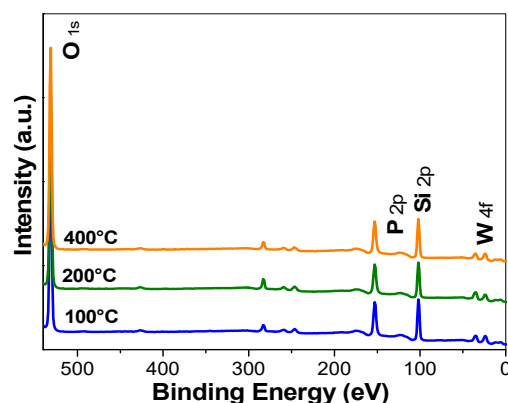
Figure 7. The XPS spectra of the 30 wt% $H_3PW_{12}O_{40}$/SBA−15 calcined at different temperature.
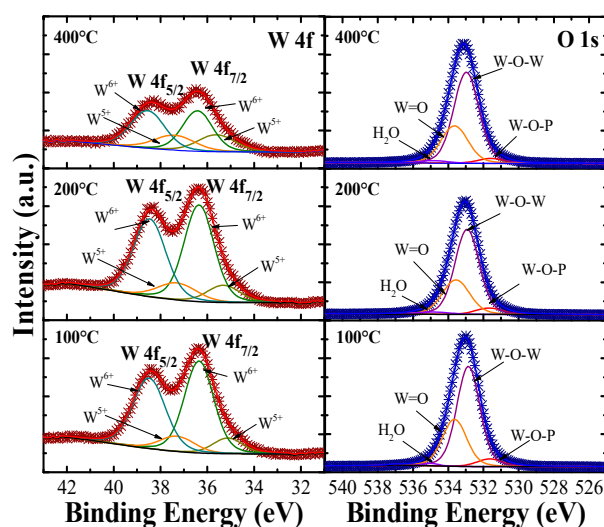
Figure 8. The W 4f and O1s core levels and their deconvolution of the XPS spectra for the 30 wt% HPW/SBA−15 calcined at different temperature.

The W 4f spectra feature two prominent peaks at 36.1 eV and 38.2 eV, corresponding to the W $4f_{5/2}$ and W $4f_{7/2}$ spin-orbit components, respectively [45]. The deconvolution of these W peaks further reveals the coexistence of W^{6+} and W^{5+} oxidation states. For example, in the 20 wt% HPW/SBA−15 catalyst, the $W^{5+}/(W^{5+} + W^{6+})$ ratio increases from 16.8% to 18.6% and 33.2% as the calcination temperature rises from 100 °C to 200 °C and 400 °C, respectively. The presence of W^{5+} species confirms the occurrence of oxygen vacancies within the *Keggin* structure. These oxygen defects lead to a decrease in electron cloud density around the tungsten atoms, creating an excess of positive charge on W^{6+} ions. To maintain overall charge neutrality, a portion of W^{6+} is reduced to W^{5+}. The simultaneous presence of W^{6+} and W^{5+} in the *Keggin* structure indicates the formation of lattice oxygen defects within the heteropolyacid cluster.

2.7. Catalytic Evaluation Results

2.7.1. Optimization of Reaction Parameters

The catalytic activity of the HPW/SBA−15 catalysts was assessed for the oxidative desulfurization (ODS) of dibenzothiophene (DBT) in a model diesel under various conditions. A control experiment, conducted without a catalyst and under conditions of an H_2O_2/DBT molar ratio of 2, a reaction temperature of 60 °C, and a reaction time of 60 min, resulted in a DBT conversion of just 15.5%. With the addition of formic acid at an H_2O_2/HCOOH molar ratio of 1.5, the conversion increased to 50.2%. However, achieving complete oxidation of sulfur compounds in fuel with H_2O_2 alone remains challenging, even with formic acid as a promoter. This study optimized the key reaction parameters, including the O/S molar ratio, reaction temperature, reaction time, and catalyst dosage for DBT oxidation. Although the theoretical stoichiometric O/S ratio for complete DBT oxidation is 2, practical applications often require a higher ratio due to limitations in adsorption efficiency and surface reaction kinetics. The optimal O/S ratio was determined experimentally by varying it from 2 to 10, while maintaining constant conditions (60 °C temperature, 60 min reaction time, and 1.5 mg/mL catalyst concentration). As shown in Figure 9A, at an O/S molar ratio of 2, the best-performing catalysts, 20 wt% and 30 wt% HPW/SBA−15, achieved maximum DBT conversions of 75.3% and 75.7%, respectively, after 60 min. Increasing the O/S ratio to 4, 6, and 8 resulted in enhanced DBT conversions of 89.2%, 94.3%, and 94.7%, respectively, for the 30 wt% HPW/SBA−15 catalyst. However, when the O/S ratio exceeded 8, a slight decrease in DBT conversion was observed. This decline is likely due to the introduction of excess water from the aqueous hydrogen peroxide solution (30 wt% in H_2O_2) and water produced during the oxidation reaction. These

water molecules can adsorb on the catalyst's active sites, impeding the interaction between the oxidant and DBT, thereby suppressing ODS efficiency. Although increasing the H_2O_2 dosage generates more hydroxyl radicals ($^\bullet OH$), which accelerate the reaction, it can also lead to the formation of perhydroxyl radicals ($^\bullet HO_2$) through the following reaction:

$$H_2O_2 + {^\bullet OH} \rightarrow H_2O + {^\bullet HO_2} \tag{1}$$
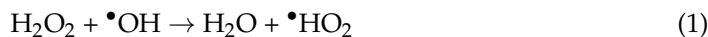
Since perhydroxyl radicals have a lower redox potential than hydroxyl radicals [46,47], the optimal O/S ratio of 8 was selected for further experiments, balancing operational costs and ODS efficiency.
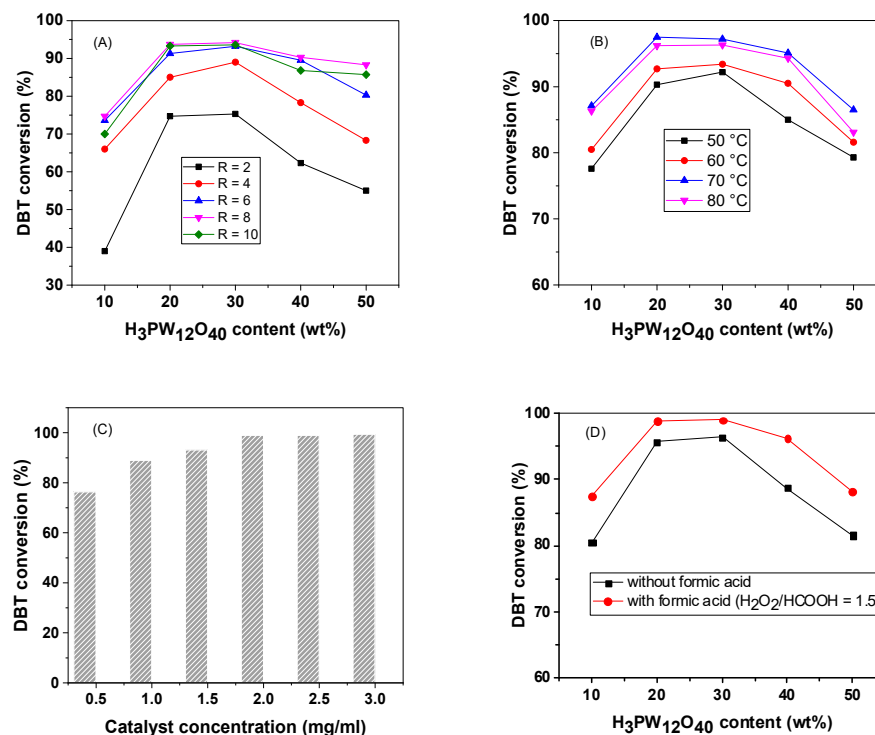
Figure 9. Effect of different reaction parameters on DBT conversion. (**A**) Effect of O/S molar ratio; (**B**) effect of reaction temperature; (**C**) effect of 20 wt% HPW/SBA−15 catalyst concentration; (**D**) effect of formic acid addition with 20 wt% HPW/SBA−15 catalyst.

The effect of reaction temperature on DBT oxidation was examined with an O/S ratio of 8, a reaction time of 60 min, and a catalyst concentration of 1.5 mg/mL (Figure 9B). As the temperature increased from 50 °C to 70 °C, the DBT conversion reached a 96.7% maximum using the best 20 wt% HPW/SBA−15 catalyst. However, at 80 °C, the conversion slightly decreased to 92.1%, likely due to partial decomposition of the oxidant and evaporation of the acetonitrile extraction agent (boiling point approximately 81.1 °C). These factors negatively impacted DBT oxidative removal, making 70 °C the optimal temperature for this reaction.

The influence of catalyst concentration on DBT oxidation was also evaluated (Figure 9C), with the highest conversion observed at a catalyst concentration of 2 mg/mL. The heteropoly-acid content in the catalysts significantly influenced DBT oxidation, with optimal phospho-tungstic acid loadings between 20 and 30 wt%. Higher loadings may result in poor dispersion and lower surface area (Table 2), both of which are detrimental to the ODS reaction. In the presence of formic acid, the DBT conversion using the 20 wt% HPW/SBA−15 catalyst significantly increased to 98.0% (Figure 9D). This enhancement is attributed to the formation of active species such as peroxometallics and superoxometallics. Experimental results confirmed

that in the presence of formic acid and H_2O_2, formic acid is oxidized to peroxyformic acid (HC=OOOH) by H_2O_2 [48,49]:

$$HCOOH + H_2O_2 \rightarrow HCOOOH + H_2O \qquad (2)$$
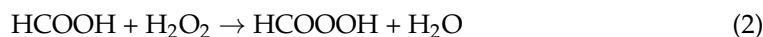
The in situ generated peroxyformic acid coordinates with the defective W^{6+} ions on the catalyst surface, forming a surface peroxophosphotungstate complex (W^{6+}–O–O–CHO). The released proton (H^+) may integrate to the Brønsted acid sites, enhancing the catalytic activity. This peroxophosphotungstate complex is more active than the symmetrical H–O–O–H species, facilitating the transfer of oxygen atoms to the sulfur atom in DBT, thereby promoting the ODS reaction [50]. Bertleff and coworkers reported that, using O_2 as oxidant and homogeneous $H_8PV_5Mo_7O_{40}$ as catalyst under moderate pressure (20 atm) and acidic condition (pH = 0.8–2) during the DBT oxidative removal procedure, in situ formed carboxylic acid, such as formic acid, showed a negative effect on DBT oxidation [51]. The authors proposed that the presence of formic acid in the aqueous catalyst phase stabilized the V-substituted species in the V^{5+} oxidation state prior to the desulfurization reaction, which resulted in an inhibition of the desulfurization reaction. In our experiments, such an inhibition effect was not observed, and formic acid did not exist as its initial state but principally in peroxophosphotungstate complex. These results indicate that the formic acid addition (this work) or formation during the reaction [51] may serve as promotor or inhibitor in the organosulfur oxidation reactions, depending on the reaction conditions (oxidant, reaction temperature, pressure) and catalysts.

2.7.2. Effect of Fuel Composition on DBT Removal

The composition of diesel fuel significantly impacts the oxidative desulfurization of dibenzothiophene (DBT). Nitrogen-containing compounds, such as indole, exhibit a stronger basic character and higher electron density compared to DBT, leading to competitive adsorption on the catalyst's active sites, particularly the Lewis acid sites and oxygen defects. Indole, with its pyridinyl nitrogen atom, can compete for these sites, potentially reducing the availability of active sites for DBT adsorption. If the catalyst has a sufficient number of active sites to accommodate both DBT and indole, the presence of indole may not significantly affect DBT removal. However, when the catalyst mass is limited, the competition between DBT and indole becomes more pronounced, resulting in a reduction of DBT conversion by approximately 7% within a 60 min reaction time (Figure 10). Our results are in good agreement with the observation reported by Rajendran A. et al. [52]. To the contrary, the other investigators claimed that by adding a proper amount of 1-methylindole, the DBT oxidation was promoted, which was explained by the formation of highly catalytically active species in the vanadium-substituted heteropolyacids catalyst, because 1-methylindole acts as a reducing agent [53]. This may be true when molecular oxygen is used as oxidant and the ODS reactions are carried out at higher pressure. However, under the same condition, addition of 2- and 3-methylindole exhibited a negative effect on DBT oxidation. These opposite observations are not fully understood yet.

When a model fuel containing 150 ppm of 4,6-dimethyldibenzothiophene (4,6-DMDBT) and 150 ppm of DBT was tested, the DBT conversion was only slightly affected, contrary to what might be expected based on competitive adsorption theory. Despite 4,6-DMDBT having a higher electron density (5.760) compared to DBT (5.758) [54], which theoretically should favor its adsorption, the conversion of DBT was not significantly diminished. The higher electron density in 4,6-DMDBT is attributed to the electron-donating methyl groups attached to the aromatic ring. However, Otsuki et al. reported that 4,6-DMDBT exhibits higher oxidation reactivity with hydrogen peroxide and formic acid than DBT, with a reaction-rate constant ratio of 1.7:1 [54]. This seemingly paradoxical result can be explained by steric hindrance from the methyl groups at the 4 and 6 positions on the aromatic rings of 4,6-DMDBT, which restricts the access of the sulfur atom to the catalyst's active sites. Specifically, in HPW/SBA−15 catalysts, these methyl groups can hinder the adsorption of 4,6-DMDBT, despite its higher electron density. Moreover, the larger molecular size of

4,6-DMDBT (179.6 ± 3.0 cm^3) compared to DBT (147 ± 3.0 cm^3) [55] further exacerbates this steric hindrance, leading to a slight reduction in DBT conversion when 4,6-DMDBT is present.
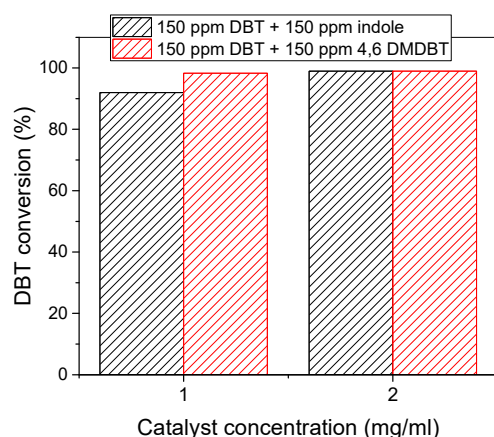
Figure 10. Effect of addition of indole and 4,6-DMDBT on the DBT oxidation using the 20 wt% HPW/SBA−15 catalyst (temperature 70 °C; catalyst concentration 2 mg/mL; R = 8; and H$_2$O$_2$/formic acid molar ratio = 1.5).

The effect of fuel composition on DBT removal was further investigated using cyclohexene and p-xylene as representatives of olefins and aromatic compounds, respectively. Experiments were conducted using (i) 95 vol% n-hexadecane with 5 vol% p-xylene and (ii) 95 vol% n-hexadecane with 5 vol% cyclohexene. As shown in Figure 11, the addition of 5 vol% p-xylene had a negligible impact on ODS activity, with DBT conversion remaining high at 98.8%. In contrast, the addition of 5 vol% cyclohexene significantly reduced DBT conversion to 91.7%, indicating that cyclohexene has a more pronounced inhibitory effect on the ODS reaction compared to p-xylene. This inhibition can be attributed to the competitive reactions between DBT and olefins, which are more susceptible to oxidation under strong oxidizing conditions, thereby hindering the ODS process.
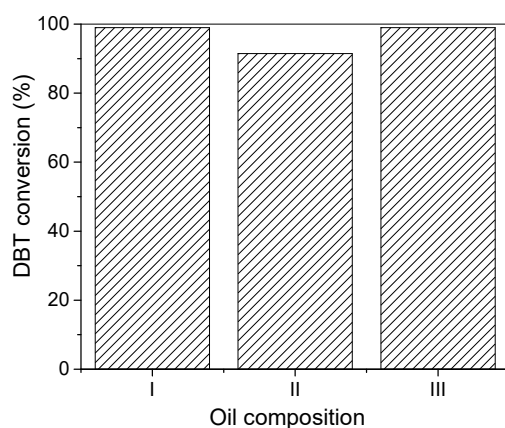
Figure 11. Effect of oil composition on DBT conversion under optimal reaction condition (temperature 70 °C; catalyst concentration 2 mg/mL; R = 6; and H$_2$O$_2$/formic acid molar ratio = 1.5). (I) 300 ppm DBT in n-hexadecane; (II) 300 ppm DBT in 95 vol% n-hexadecane + 5 vol% p-xylene; (III) 300 ppm DBT in 95 vol% n-hexadecane + 5 vol% cyclohexene.

2.7.3. Correlation of Oxygen Defects and Surface Acidity with Catalytic Activity

Characterization through in situ FTIR spectroscopy of pyridine adsorption reveals that HPW/SBA−15 catalysts are predominantly characterized by Lewis acid sites. DBT molecules, which contain sulfur atoms with two pairs of unshared electrons, can act as

Lewis bases by donating electrons to these Lewis acid sites on the catalyst. During the oxidative desulfurization reaction, DBT preferentially adsorbs onto these sites via acid–base interactions, where the sulfur atom in DBT donates its electron pairs to the catalyst's Lewis acid sites. This observation aligns with previous studies on supported transition metal oxides, such as MoO_3/SBA−15 [21] and V_2O_5/SBA−15 [22], which exhibit similar behavior. The *Keggin* structure within the HPW/SBA−15 catalyst shows structural defects, as confirmed by in situ FTIR and Rietveld structure refinement analyses. These defects are primarily due to the rupture of W–O_c–W and W=O_t bonds, which occur during calcination-induced surface dehydroxylation. The resulting oxygen deficiencies decrease the electron density around the tungsten (W) ions, making these ion electron acceptors maintain charge neutrality. W^{6+} electron configurations with unoccupied 3d orbitals also serve as electron acceptors. Therefore, tungsten ions with oxygen defects or coordinately unsaturated W^{6+} species in the HPW/SBA−15 catalysts are a significant source of Lewis acid sites.

Oxidants such as H_2O_2 or peroxyformic acid (HCOOOH), which possess unpaired electrons, can adsorb onto W^{6+} ions with oxygen defects or Lewis acid sites, forming active species like peroxometallics and superoxometallics. Both DBT and these oxidants preferentially adsorb onto these sites, leading to competition that enhances the transfer of oxygen from the peroxometallic and superoxometallic species to the sulfur atom in DBT, ultimately promoting the formation of $DBTO_2$ sulfone. Figure 12 illustrates the relationship between the relative intensity of the W=O band (I_{980}) and the number of Lewis acid sites in the 10–30 wt% HPW/SBA−15 catalysts as a function of temperature. The decrease in W=O band intensity with increasing temperature indicates a greater number of oxygen defects within the *Keggin* structure. Conversely, the number of Lewis acid sites increases with higher calcination temperatures, suggesting that the formation of oxygen defects from the rupture of W=O and corner-sharing W–O_c–W bonds at elevated temperatures contributes to the generation of additional Lewis acid sites. The relationship between DBT conversion and surface acidity is further explored in Figure 13, which presents plots of Lewis acid sites, Brønsted acid sites, total acidity, and DBT conversion against the heteropolyacid loading of the catalysts. Under optimal reaction conditions, DBT conversion shows a strong correlation with the number of Lewis acid sites and the total acidity. However, higher heteropolyacid content introduces more oxygen defects into the *Keggin* structure, potentially enhancing DBT adsorption. This effect is counterbalanced by a reduction in surface area, poorer heteropolyacid dispersion, and partial pore blockage within the SBA−15 framework, which results in fewer exposed acid sites and decreased DBT oxidation efficiency. These findings suggest that surface Lewis acidity and total acidity are critical factors in DBT oxidation. A synergistic interaction between Brønsted and Lewis acid sites likely facilitates the transfer of oxygen between peroxometallic and superoxometallic species and DBT, which will be further elaborated upon in the proposed reaction mechanisms.
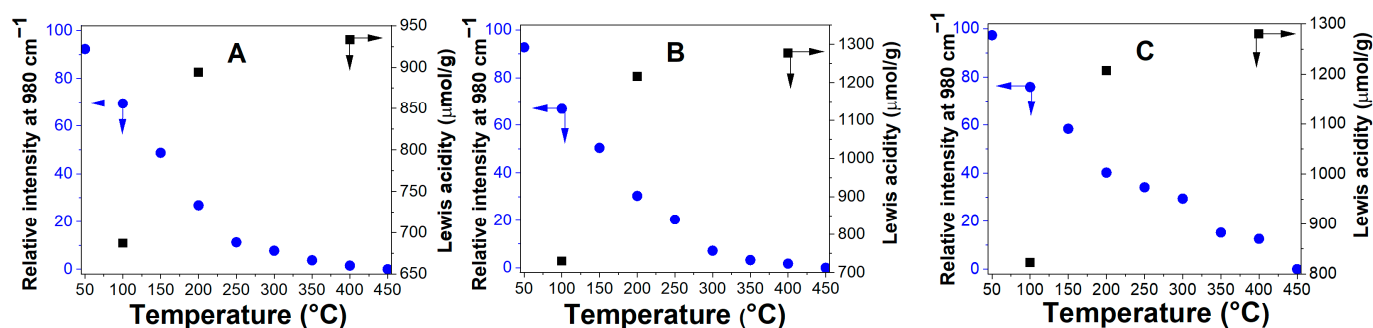
Figure 12. The relative intensity of the IR band at 980 cm^{-1} and Lewis acidity of the $H_3PW_{12}O_{40}$/SBA−15 catalyst were plotted as a function of treatment temperature. (**A**) 10 wt% $H_3PW_{12}O_{40}$/SBA−15; (**B**) 20 wt% $H_3PW_{12}O_{40}$/SBA−15; (**C**) 30 wt% $H_3PW_{12}O_{40}$/SBA−15.
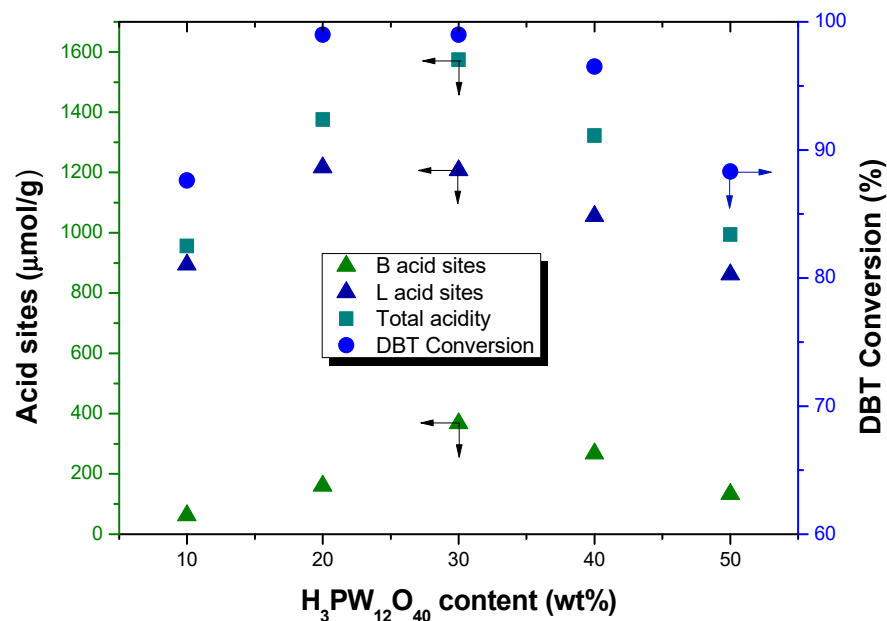
Figure 13. Variation of acidity and DBT conversion with the $H_3PW_{12}O_{40}$ content in $H_3PW_{12}O_{40}$/SBA−15 catalysts calcined at 200 °C. The acidity data were obtained from FTIR of pyridine adsorption at 100 °C. The DBT conversion was obtained in the presence of formic acid under the reaction conditions: temperature 70 °C; O/S molar ratio 8; reaction time 60 min; catalyst concentration 2 mg/mL.

2.7.4. Catalytic Mechanisms

Building upon the results and discussions presented, we propose a detailed mechanism for the oxidative desulfurization (ODS) reaction involving the formation of peroxotungstate species, the nucleophilic attack by the sulfur atom in DBT, and the critical role of surface acidity. For the most effective catalysts, namely, 20–30 wt% HPW/SBA−15 calcined at 100 and 200 °C, oxygen defects do not appear to be the primary factor driving DBT adsorption and oxidation. Therefore, the proposed mechanism for these catalysts, illustrated in Scheme 1, excludes the influence of oxygen defects. In this mechanism, the oxidant (H_2O_2) adsorbs onto the catalyst's surface, oxidizing the exposed W=O bonds to form a surface peroxophosphotungstate complex (W–O–O–W). Concurrently, DBT in the fuel adsorbs onto the catalyst's Lewis acid sites, where it facilitates the transfer of an oxygen atom from the peroxophosphotungstate complex to the sulfur atom in DBT, resulting in the formation of sulfone ($DBTO_2$). Alternatively, DBT can directly interact with the O–O bond in the complex, achieving the same oxidation outcome.

For the sample calcined at 400 °C, more oxygen defects are created in the *Keggin* structure. In such a situation, in the presence of formic acid, the in situ formed peroxyformic acid could not only coordinate with the oxygen defects, but also attack the W=O bond in the *Keggin* structure to generate a surface peroxophosphotungstate complex (W^{6+}–O–O–CHO), as demonstrated in Scheme 2. The H^+ proton in the peroxophosphotungstate complex interacts with B acid sites to enhance the electron cloud deformation around the O–O bond, favoring the O atom transfer from W–O–O–CHO by O–O bond cleavage. As a result, one $[HCOO]^-$ species and sulfoxide or sulfone were formed; B acid sites may donate an H^+ to $[HCOO]^-$ species to form a formic acid molecule. Thus, the ODS reaction cycle was complete. In this procedure, both L and B acid participated in the ODS reaction; however, they took different roles: L acid served as active sites for DBT adsorption and peroxophosphotungstate complex formation, while B acid sites assisted in the O atom and H^+ transfer between the adsorbed DBT and peroxophosphotungstate complex.
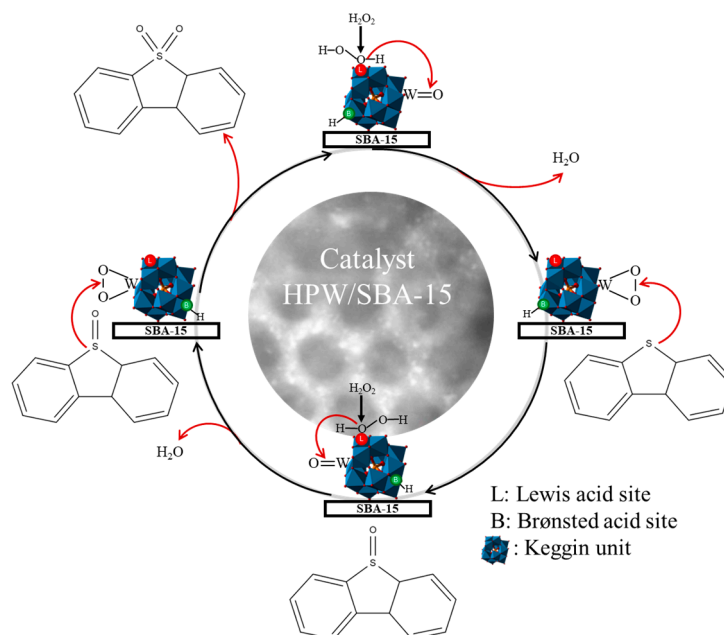
Scheme 1. An ODS reaction mechanism on the 20–30 wt%$H_3PW_{12}P_{40}$/SBA−15 catalysts calcined at 200 °C where the oxygen atom transfers mainly via nucleophilic attack of the sulfur atom in DBT towards the peroxotungstate species in the *Keggin* structure.
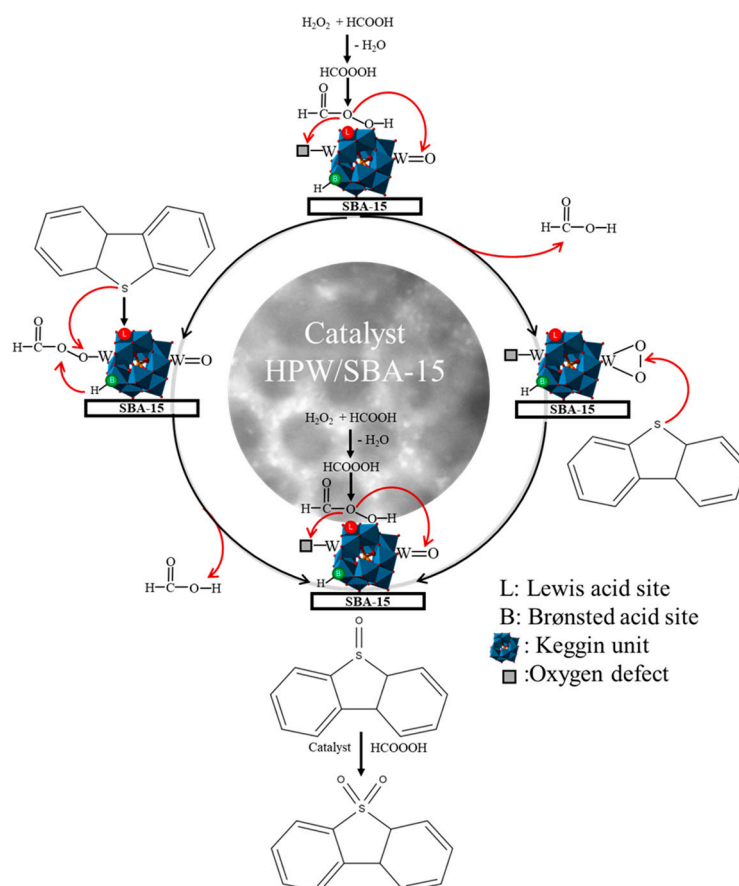
Scheme 2. An ODS reaction mechanism on the $H_3PW_{12}P_{40}$/SBA−15 catalyst calcined at 400 °C. The DBT oxidation reaction may simultaneously occur in both oxygen defects in the *Keggin* structure and peroxophosphotungstate complex.

2.7.5. Catalyst Reusability

The reusability of the 30 wt% HPW/SBA−15 catalyst was evaluated by measuring the conversion of DBT across six successive reaction cycles, with the catalyst's stability assessed by monitoring potential metal leaching into the oil and solvent phases after each cycle. The metal concentrations in these phases were determined using inductively coupled plasma mass spectrometry (ICP-MS), with precise measurements conducted using a PerkinElmer/Sciex ELAN Dynamic Reaction Cell (DRCPlus) coupled with a PerkinElmer AS-93 Plus Autosampler. Considering that some catalyst mass loss might occur during the separation process, potentially affecting DBT oxidation, consistent ratios of oil volume to catalyst mass were maintained throughout the tests. The results, illustrated in Figure 14, show that DBT conversion remained nearly constant during the first three reaction cycles. However, a gradual decline in catalytic activity was observed from the fourth to the fifth cycles, with DBT conversion decreasing to 96.4% and 95.1%, respectively.
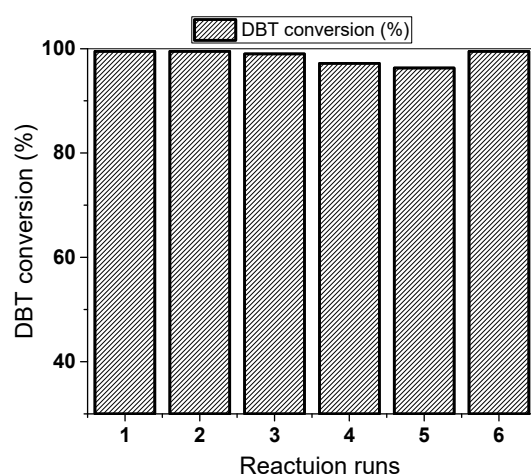
Figure 14. The reusability test of the best 20 wt% HPW/SBA−15 catalyst under the optimal reaction conditions (temperature 70 °C; catalyst concentration 2 mg/mL; O/S = 8; and H_2O_2/formic acid molar ratio = 1.5).

ICP-MS analysis revealed no detectable leaching of W^{6+} into either the oil or extracted phases after five reaction cycles, indicating that the catalyst structure remained largely intact. To regenerate the catalyst, the spent samples were thoroughly washed with acetonitrile and then dried before being tested in the sixth reaction cycle. Remarkably, the DBT conversion in this sixth cycle rebounded to 99%, matching the performance of the fresh catalyst. These findings suggest that the decline in catalytic activity observed after repeated cycles is likely due to the occupation of active sites on the catalyst surface by adsorbed DBT or sulfone products. However, this loss of activity can be effectively restored by washing the used catalyst with acetonitrile, which removes these adsorbed species and rejuvenates the catalyst's performance. This highlights the robustness and recyclability of the HPW/SBA−15 catalyst in oxidative desulfurization processes.

3. Experimental

3.1. SBA−15 and $H_3PMo_{12}O_{40}$/SBA−15 Synthesis

The SBA−15 was synthesized using the hydrothermal method as described in the literature [19]. In this process, tetraethyl orthosilicate (TEOS, Sigma-Aldrich, St. Louis, MO, USA) was employed as the silicon precursor, and a [(polyethylene oxide)–block-(polypropylene oxide)–block-(polyethylene oxide)] triblock copolymer (Pluronic P123, Sigma-Aldrich, St. Louis, MO, US) was used as a template. The $H_3PW_{12}O_{40}$/SBA−15 catalysts were prepared via the incipient wetness impregnation method. Specifically, 5 g of SBA−15 was impregnated with 100 mL of methanol (Fermont, MTY, MX), maintaining a methanol-to-SBA−15 ratio of 20 mL/g. The methanol solution contained a calculated

amount of $H_3PW_{12}O_{40}$ (Sigma-Aldrich, St. Louis, MO, US) to achieve the desired loading, varying from 10 to 50 wt% of $H_3PW_{12}O_{40}$ on the SBA$-$15 support. The resulting suspension was transferred to a rotary evaporator and placed inside a water bath at 50 °C to evaporate the methanol completely. The dried solid obtained from this process was then divided into three portions: one third was dried at 100 °C, another third was calcined at 200 °C for 2 h, and the final third was calcined at 400 °C for 2 h. The prepared samples were labeled as xHPW/SBA$-$15, where "x" denotes the $H_3PW_{12}O_{40}$ content, and HPW refers to $H_3PW_{12}O_{40}$.

3.2. Characterization

X-ray diffraction (XRD) patterns were recorded using a diffractometer (D500 diffractometer, Siemens, Fort Worth, TX, USA), scanning across a 2θ range of 10 to 70° with a step size of 0.02° and a scanning speed of 2.4°/min. The textural properties of the samples were determined using nitrogen (N_2) adsorption–desorption isotherms at -196 °C, measured with a Nova 4200e Series instrument (Quantachrom Instruments, Boynton Beac, FL, USA) Prior to analysis, each sample was subjected to thermal treatment at 200 °C for 12 h under vacuum. The specific surface area was calculated using the Brunauer–Emmett–Teller (BET) model, while pore size distribution was determined using the Barrett–Joyner–Halenda (BJH) model. Morphological features and particle size distribution of the catalysts were examined by transmission electron microscopy (TEM) using a microscope (JEM-ARM200 CF, JEOL Ltd., Tokyo, Japan) operated at an accelerating voltage of 200 kV. Selected areas in the TEM images were analyzed by energy-dispersive X-ray spectroscopy (EDS) to determine the elemental composition of the nanoparticles.

X-ray photoelectron spectroscopy (XPS) analyses were conducted using a spectrometer (K-Alpha, Thermo Fisher Scientific Inc., Waltham, MA, USA) equipped with a monochromatic Al Kα source (1478 eV). The analysis area was 400 μm^2, and a charge neutralizer was employed. The sample powders were dispersed on a carbon film and affixed to the sample holder using double-sided copper tape. The structure and stability of the HPW/SBA$-$15 catalysts were investigated using in situ Fourier-transform infrared (FTIR) spectroscopy. Measurements were performed with a PerkinElmer Model 170-SX FTIR spectrometer (Waltham, MA, USA). A solid wafer (1 cm in diameter, approximately 10–20 mg in mass) was placed on a glass support within an IR cell. The temperature was increased at a rate of 5 °C/min under vacuum conditions (10^{-5} torr). IR spectra were recorded at various temperatures: 25, 50, 100, 150, 200, 250, 300, 350, 400, and 450 °C.

3.3. Surface Acidity Measurements

The surface acidity of the samples was determined using an in situ Fourier-transform infrared (FTIR) spectroscope (170-SX, PerkinElmer, Waltham, MA, USA) with the pyridine adsorption method. Before pyridine exposure, the sample wafer was activated by heating at 200 °C for 1 h under vacuum (10^{-5} torr) to remove any adsorbed surface species. After cooling to room temperature, approximately 10 μL of liquid pyridine was introduced into the IR cell containing the solid wafer. The pyridine was allowed to adsorb onto the sample surface for 15 min at the set temperature, after which excess pyridine was removed by vacuum. IR spectra were recorded over a temperature range of 50 to 400 °C to monitor the interactions between the adsorbed pyridine molecules and the surface acid sites of the catalysts. Characteristic IR bands in the 1300–1700 cm^{-1} region were analyzed to distinguish between Brønsted and Lewis acid sites. The presence of pyridinium ions adsorbed on Brønsted acid sites was indicated by an IR band at 1545 cm^{-1}, while coordinated pyridine on Lewis acid sites was identified by an IR band at approximately 1455 cm^{-1}. The concentration of surface acidity was calculated using the Beer–Lambert law:

$$C = (AS/\varepsilon m) \times 1000, \tag{3}$$

where C is the acid sites concentration ($\mu mol/gcat$), A is the IR band's area (absorption cm^{-1}), S is the wafer surface (cm^2), m corresponds to the wafer mass (mg), and ε is the molar

extinction coefficient (cm.μmol^{-1}). The extinction coefficients, EB = 1.0086 mmol/cm^2 for Brønsted acid sites and EL = 0.9374 mmol/cm^2 for Lewis acid sites, were used for the acidity data calculation. The extinction coefficient is a measure of how strongly a chemical species attenuates light at a given wavelength, which is described in the Supplementary Materials.

3.4. Structure Refinement with Rietveld Method

The crystalline structures of the catalysts were refined using the Rietveld method, employing the JAVA-based software Version 2.998 Materials Analysis Using Diffraction (MAUD) [56]. The concentration of oxygen defects in the dispersed $H_3PW_{12}O_{40}$ crystals was determined by refining the occupancy of oxygen atoms within the *Keggin* structure. The oxygen defect concentration was calculated using the following equa, tion:

$$\text{Oxygen defect (\%)} = (O_{tn} - O_{rn})/O_{tn}, \tag{4}$$

where O_{tn} is the theoretical occupancy number of oxygen atoms in the unit lattice cell of ideal $H_3PW_{12}O_{40}$ crystal, and O_{rn} is the real occupancy number of oxygen atoms in the unit lattice cell in the dispersed $H_3PW_{12}O_{40}$ crystals on the SBA−15 support. For the structural refinement, the H, O, P, and W atomic fractional coordinates, crystal space group, structure symmetry, and theoretical occupancy number in the orthorhombic and cubicstructures of $H_3PW_{12}O_{40}$ are reported in SM Tables S1 and S2 in the Supplementary Materials. The weighted-profile R factors (R_{wp}) are not estimates of the probable errors in the analysis as a whole, but only of minimum possible errors based on normal distribution.

For the structural refinement, the atomic fractional coordinates for hydrogen (H), oxygen (O), phosphorus (P), and tungsten (W), as well as the crystal space group, structural symmetry, and theoretical occupancy numbers for the orthorhombic structure of $H_3PW_{12}O_{40}$, were referenced as reported in Table S1 of the Supplementary Materials. The weighted-profile R factors (R_{wp}) were used as indicators of the refinement quality; these factors are not estimates of the overall errors but represent the minimum possible errors based on a normal distribution.

3.5. Catalytic Evaluation

The catalytic activity of the catalysts was assessed using the oxidation of dibenzothiophene (DBT) as a model reaction. The reaction mixture consisted of 300 ppm DBT dissolved in n-hexadecane, representing model diesel fuel. To investigate the impact of fuel composition on oxidative desulfurization (ODS) efficiency, cyclohexene and p-xylene were selected as representative olefins and aromatic compounds commonly found in real diesel fuel. These compounds were mixed with n-hexadecane to create three different model diesel mixtures: (i) 95 vol% n-hexadecane and 5 vol% p-xylene, (ii) 95 vol% n-hexadecane and 5 vol% cyclohexene, and (iii) 90 vol% n-hexadecane, 5 vol% cyclohexene, and 5 vol% p-xylene. To further explore the influence of other fuel components on ODS efficiency and potential reaction competition, some experiments included alkylated DBT derivatives, such as 4,6-dimethyldibenzothiophene (4,6-DMDBT), and nitrogen-containing compounds like indole mixed with DBT in the reaction mixture.

The oxidation reactions were carried out under atmospheric pressure at varying temperatures of 50, 60, 70, and 80 °C, with a reaction time of 60 min and an agitation speed of 750 rpm. Hydrogen peroxide (H_2O_2) was used as the oxidant, with a molar ratio of H_2O_2/DBT ranging from 2 to 10. In certain experiments, formic acid (HCOOH) was added to the H_2O_2 to enhance its stability and oxidation power. The H_2O_2/HCOOH molar ratio was maintained at 1.5, and the mixture was added to the reaction system in three portions to prevent rapid heat release—one third at the beginning, another third after 20 min, and the final third after 40 min of reaction. The effect of catalyst concentration on the ODS reaction was evaluated by varying the catalyst amount from 0.5 to 3 mg/mL. DBT concentration in the n-hexadecane phase was analyzed using UV–Vis spectrophotometry. The absorption band at 240 nm was monitored to track changes in DBT concentration, while the absorption bands at approximately 212 nm and 235 nm were used to detect

the formation of sulfoxide and sulfone, respectively. The conversion of DBT (X_DB) was calculated using the following equation:

$$X_{DBT} \, (\%) = (C_0 - C_t)/C_0, \tag{5}$$

where X_{DBT} is the DBT conversion or oxidative removal, C_0 is the DBT concentration in the oil phase at time zero, and C_t is the DBT concentration in the oil phase at time t. The volume of the reaction mixture was assumed to be constant, as only a very small liquid sample was withdrawn from the reaction mixture for analysis.

4. Conclusions

This study successfully demonstrated an effective strategy for the simultaneous oxidation and separation of refractory organosulfur compounds, such as dibenzothiophene (DBT) and 4,6-dimethyldibenzothiophene (4,6-DMDBT), from model diesel fuel. Using a biphasic system with hydrogen peroxide as the oxidant and defective heteropolyoxometalate catalysts, the approach shows significant potential for achieving ultra-clean diesel fuel with near-zero sulfur content. The investigation provided an in-depth analysis of oxygen defects within the *Keggin* structure of the dispersed HPW/SBA−15 catalysts, using techniques such as Rietveld structural refinement, in situ FTIR characterization, and XPS analysis. The results revealed that these oxygen defects are influenced by calcination temperature and heteropolyacid content. The presence of Lewis acid sites in the catalysts was found to be critical, serving a dual function: accepting the lone electron pairs of sulfur atoms in DBT molecules and acting as active centers for the formation of surface peroxometallic species. Additionally, Brønsted acid sites facilitated the transfer of oxygen between the oxidant and peroxometallic species, thereby promoting the conversion of sulfur compounds to sulfones.

The HPW/SBA−15 catalysts exhibited outstanding catalytic activity for DBT oxidation, particularly in the presence of H_2O_2 and formic acid. Under optimal reaction conditions (70 °C, 60 min reaction time, O/S molar ratio of 6–8, H_2O_2/formic acid molar ratio of 1.5, and catalyst concentration of 2 mg/mL), more than 99% of DBT was effectively oxidized and separated from the oil phase. However, the presence of compounds such as cyclohexene and indole in the model diesel negatively impacted DBT oxidation, leading to a reduction in DBT conversion. The best catalytic performance was observed in the 20–30 wt% HPW/SBA−15 catalysts. This superior performance can be attributed to their higher concentration of Lewis and Brønsted acid sites, greater dispersion, and more pronounced defects within the *Keggin*-type heteropolyoxometalate structure. These findings underscore the importance of optimizing the structural and compositional parameters of the catalysts to maximize their effectiveness in oxidative desulfurization processes, paving the way for cleaner diesel production.

Cooperation and Exchange Office at the East China University of Science and Technology in China is also appreciated.

Conflicts of Interest: The authors declare no conflicts of interest.

References

1. Taschner, K. Environmentalists' review on automotive exhaust gases. In *Catalysis and Automotive Pollution Control II, Studies in Surface Science and Catalysis*; Crucq, A., Ed.; Elsevier: Amsterdam, The Netherlands; Oxford, UK; New York, NY, USA; Tokyo, Japan, 1991; Volume 71, pp. 5–15.
2. Stanislaus, A.; Marafi, A.; Rana, M.S. Recent advances in the science and technology of ultra-low sulfur diesel (ULSD) production. *Catal. Today* **2010**, *153*, 1–68. [CrossRef]
3. Babich, J.A.; Moulijn, J.A. Science and technology of novel processes for deep desulfurization of oil refinery streams: A review. *Fuel* **2003**, *82*, 607–631. [CrossRef]
4. Song, C.S. An overview of new approaches to deep desulfurization for ultra-clean gasoline, diesel fuel and jet fuel. *Catal. Today* **2003**, *86*, 211–263. [CrossRef]
5. Pawelec, B.; Navarro, R.M.; Campos-Martin, J.M.; Fierro, J.L.G. Towards near zero-sulfur liquid fuels: A perspective review. *Catal. Sci. Technol.* **2001**, *1*, 23–42. [CrossRef]
6. Castillo, P.; Ramírez, J.; Cuevas, R.; Vázquez, P.; Castaneda, R. Influence of the support on the catalytic performance of Mo, CoMo, and NiMo catalysts supported on Al_2O_3 and TiO_2 during the HDS of thiophene, dibenzothiophene, or 4,6-dimethyldibenzothiophene. *Catal. Today* **2016**, *259*, 140–149. [CrossRef]
7. Prince, R.C.; Grossman, M.J. Substrate preferences in biodesulfurization of diesel range fuels by *Rhodococcus* sp. Strain ECRD-1. *Appl. Environ. Microbiol.* **2003**, *69*, 5833–5838. [CrossRef]
8. Maghsoudi, S.; Vossoughi, M.; Kheirolomoom, A.; Tanaka, E.; Katoh, S. Biodesulfurization of hydrocarbons and diesel fuels by *Rhodococcus* sp. strain P32C1. *Biochem. Eng. J.* **2001**, *8*, 151–156. [CrossRef]
9. Yang, J.; Hu, Y.; Zhao, D.; Wang, S.; Lau, P.C.K.; Marison, I.W. Two-layer continuous-process design for the biodesulfurization of diesel oils under bacterial growth conditions. *Biochem. Eng. J.* **2007**, *37*, 212–218. [CrossRef]
10. Yu, G.X.; Jin, M.; Sun, J.; Zhou, X.L.; Chen, L.F.; Wang, J.A. Oxidative modifications of rice hull-based carbons for dibenzothiophene adsorptive removal. *Catal. Today* **2013**, *212*, 31–37. [CrossRef]
11. Timko, M.T.; Wang, J.A.; Burgess, J.; Kracke, P.; Gonzalez, L.; Jaye, C.; Fischer, D.A. Roles of surface chemistry and structural defects of activated carbons in the oxidative desulfurization of benzothiophenes. *Fuel* **2016**, *163*, 223–231. [CrossRef]
12. Gonzlez, L.A.; Kracke, P.; Green, W.H.; Tester, J.W.; Shafer, L.M.; Timko, M.T. Oxidative Desulfurization of Middle-Distillate Fuels Using Activated Carbon and Power Ultrasound. *Energy Fuels* **2012**, *26*, 5164–5176. [CrossRef]
13. Wei, S.; He, H.; Cheng, Y.; Yang, C.; Zeng, G.; Qiu, L. Performances, kinetics and mechanisms of catalytic oxidative desulfurization from oils. *RSC Adv.* **2016**, *6*, 103253–103269. [CrossRef]
14. Campos-Martin, J.M.; Capel-Sanchez, M.C.; Perez-Presas, P.; Fierro, J.L.G. Oxidative processes of desulfurization of liquid fuels. *J. Chem. Technol. Biotechnol.* **2010**, *85*, 879–890. [CrossRef]
15. Yan, X.M.; Mei, P.; Xiong, L.; Gao, L.; Yang, Q.; Gong, L. Mesoporous titania-silica- polyoxometalate nanocomposite materials for catalytic oxidation desulfurization of fuel oil. *Catal. Sci. Technol.* **2013**, *3*, 1985–1992. [CrossRef]
16. Ma, X.L.; Zhou, A.N.; Song, C.S. A novel method for oxidative desulfurization of liquid hydrocarbon fuels based on catalytic oxidation using molecular oxygen coupled with selective adsorption. *Catal. Today* **2007**, *123*, 276–284. [CrossRef]
17. Wang, D.; Qian, E.W.; Amano, H.; Okata, K.; Ishihara, A.; Kabe, T. Oxidative desulfurization of fuel oil Part I. Oxidation of dibenzothiophenes using tert-butyl hydroperoxide. *Appl. Catal. A* **2003**, *253*, 91–99. [CrossRef]
18. De Filipps, P.; Scarsella, M. Functionalized hexagonal mesoporous silica as an oxidizing agent for the oxidative desulfurization of oorganosulfur compounds. *Ind. Eng. Chem. Res.* **2008**, *47*, 973–975. [CrossRef]
19. Eseva, E.A.; Lukashov, M.O.; Cherednichenko, K.A.; Levin, I.S.; Akopyan, A.V. Heterogeneous catalysts containing an Anderson-type polyoxometalate for the aerobic oxidation of sulfur-containing compounds. *Ind. Eng. Chem. Res.* **2021**, *60*, 14154–14165. [CrossRef]
20. Anderson, K.; Arkins, M.P.; Borges, P.; Chern, Z.P.; Rafeen, M.S.; Sebran, N.H.; Vander Pool, E.; Vleeming, J.H. Economic analysis of ultrasound-assisted oxidative desulfurization. *Energy Sources Part B Econ. Plan. Policy* **2017**, *12*, 297–304. [CrossRef]
21. González, J.; Wang, J.A.; Chen, L.F.; Manríquez, M.E.; Limas, R.; Arrlleno, U. $MoO_3/SBA-15$ catalysts: Structural defects, surface Lewis acidity and catalytic activity. *J. Solid State Chem.* **2018**, *263*, 100–114. [CrossRef]
22. Ramos, J.M.; Wang, J.A.; Flores, S.O.; Chen, L.F.; Noreña, L.E.; Arellano, U.; González, J.; Navarrete, J. Ultrasound-assisted hydrothermal synthesis of $V_2O_5/Zr-SBA-15$ catalysts for production of ultralow sulfur fuel. *Catalysts* **2021**, *11*, 408. [CrossRef]
23. Rodriguez-Gattorno, G.; Galano, A.; Torres-García, E. Surface acid–basic properties of $WOx–ZrO_2$ and catalytic efficiency in oxidative desulfurization. *Appl. Catal. B Environ.* **2009**, *92*, 1–8. [CrossRef]
24. Taghizadeh, M.; Mehrvarz, E.; Taghipour, A. Polyoxometalate as an effective catalyst for the oxidative desulfurization of liquid fuels: A critical review. *Rev. Chem. Eng.* **2020**, *36*, 831–858. [CrossRef]

25. Granadeiro, C.M.; Ferreira, P.M.C.; Julião, D.; Ribeiro, L.A.; Valença, R.; Ribeiro, J.C.; Gonçalves, I.S.; de Castro, B.; Pillinger, M.; Cunha-Silva, L.; et al. Efficient oxidative desulfurization processes using polyoxomolybdate based catalysts. *Energies* **2018**, *11*, 1696. [CrossRef]

26. Gao, Y.; Julião, D.; Silva, D.F.; de Castro, B.; Zhao, J.; Balula, S.S. A simple desulfurization process to achieve high efficiency, sustainability and cost-effectivity via peroxotungstate catalyst. *Mol. Catal.* **2021**, *505*, 111515. [CrossRef]

27. Crawen, M.; Xiao, D.; Kunstmann-Olsen, C.; Kozhevnikova, E.F.; Blanc, F.; Steiner, A.; Kozhevnikov, I.V. Oxidative desulfurization of diesel fuel catalyzed by polyoxometalate immobilized on phosphazene-functionalized silica. *Appl. Catal. B Environ.* **2018**, *231*, 82–91.

28. Qiu, J.; Wang, G.; Zhang, Y.; Zeng, D.; Chen, Y. Direct synthesis of mesoporous $H_3PMo_{12}O_{40}/SiO_2$ and its catalytic performance in oxidative desulfurization of fuel oil. *Fuel* **2015**, *147*, 195–202. [CrossRef]

29. Du, Y.; Lei, J.; Zhou, L.; Guo, Z.R.; Li, J.; Du, X. Highly efficient deep desulfurization of fuels by meso/macroporous $H_3PW_{12}O_{40}/TiO_2$ at room temperature. *Mater. Res. Bull.* **2018**, *105*, 210–219.

30. Bertleff, B.; Claußnitzer, J.; Korth, W.; Wasserscheid, P.; Jess, A.; Albert, J. Extraction coupled oxidative desulfurization of fuels to sulfate and water-soluble sulfur compounds using polyoxometalate catalysts and molecular oxygen. *ACS Sustain. Chem. Eng.* **2017**, *5*, 4110–4118. [CrossRef]

31. Hossain, M.; Park, H.; Choi, H. A Comprehensive review on catalytic oxidative desulfurization of liquid fuel oil. *Catalysts* **2019**, *9*, 229. [CrossRef]

32. Huang, X.; Wang, W.; Liu, X. $H_3PW_{12}O_{40}$-doped pyromellitic diimide prepared via thermal transformation as an efficient visible-light photocatalyst. *J. Mater. Sci.* **2020**, *55*, 8502–8512. [CrossRef]

33. Frenzel, R.; Morales, D.; Romanelli, G.; Sathicq, G.; Blanco, M.; Pizzio, L. Synthesis, characterization and catalytic evaluation of $H_3PW_{12}O_{40}$ included in acrylic acid/acrylamide polymer for the selective oxidation of sulfides. *J. Mol. Catal. A Chem.* **2016**, *420*, 124–133. [CrossRef]

34. Sing, K.S.W.; Evertt, D.H.; Haul, R.A.W.; Moscou, L.; Pierotti, R.A.; Rouquerol, J.; Siemieniewska, T. Reporting physisorption data for gas/solid systems with special reference to the determination of surface area and porosity. *Pure Appl. Chem.* **1985**, *57*, 603–619. [CrossRef]

35. Janik, M.J.; Campbell, K.A.; Bardin, B.B.; Davis, R.J.; Neurock, M. A computational and experimental study of anhydrous phosphotungstic acid and its interaction with water molecules. *Appl. Catal. A Gen.* **2003**, *256*, 51–68. [CrossRef]

36. Ivanov, A.V.; Vasina, T.V.; Nissenbaum, V.D.; Kustov, L.M.; Timofeeva, M.N.; Houzvicka, J.I. Isomerization of n-hexane on the Pt-promoted *Keggin* and Dawson tungstophosphoric heteropoly acids supported on zirconia. *Appl. Catal. A Gen.* **2004**, *259*, 65–72. [CrossRef]

37. Zheng, H.; Sun, Z.; Chen, X.; Zhao, Q.; Wang, X.; Jiang, Z. A micro reaction-controlled phase transfer catalyst for oxidative desulfurization based on polyoxometalate modified silica. *Appl. Catal. A Gen.* **2013**, *467*, 26–32. [CrossRef]

38. Narkhede, N.; Brahmkhatri, V.; Patel, A. Efficient synthesis of biodiesel from waste cooking oil using solid acid catalyst comprising 12-tungstosilicic acid and SBA−15. *Fuel* **2014**, *135*, 253–261. [CrossRef]

39. Pham, S.T.; Nguyen, B.M.; Le, G.H.; Mutyala, A.S.S.; Szenti, I.; Konya, Z.; Tuan, A.V. Role of Brønsted and Lewis acidic sites in sulfonated Zr-MCM-41 for the catalytic reaction of cellulose into 5-hydroxymethyl furfural. *React. Kinet. Mech. Catal.* **2020**, *130*, 825–836. [CrossRef]

40. Izumi, Y.; Urabe, K.; Makoto, O. *Zeolite, Clay, and Heteropoly Acid in Organic Reactions*; Wiley-VCH: Weinheim, Germany, 1992.

41. Parry, E.P. An infrared study of pyridine adsorbed on acidic solids characterization of surface acidity. *J. Catal.* **1963**, *2*, 371–379. [CrossRef]

42. Sánchez-Valente, J.; Bokhimi, X.; Hernández, F. Physicochemical and catalytic properties of sol–gel alumina aged under hydrothermal conditions. *Langmuir* **2003**, *19*, 3583–3588. [CrossRef]

43. Chen, L.F.; Noreña, L.E.; Wang, J.A.; Zhou, X.L.; Navarrete, J.; Hernández, I.; Montoya, A.; Pérez Romo, P.; Salas, P.; Castella Pergher, S. A study of n-hexane hydroisomerization catalyzed with the $Pt/H_3PW_{12}O_{40}/Zr$-MCM-41 catalysts. *Catal. Today* **2008**, *133–135*, 331–338. [CrossRef]

44. Lia, K.; Zhong, Y.; Luo, S.; Deng, W. Fabrication of powder and modular $H_3PW_{12}O_{40}/Ag_3PO_4$ composites: Novel visible-light photocatalysts for ultra-fast degradation of organic pollutants in water. *Appl. Catal. B Environ.* **2020**, *278*, 119313. [CrossRef]

45. Newman, A.D.; Brown, D.R.; Siril, P.; Lee, A.F.; Wilson, K. Structural studies of high dispersion $H_3PW_{12}O_{40}/SiO_2$ solid acid catalysts. *Phys. Chem. Chem. Phys.* **2005**, *8*, 2893. [CrossRef] [PubMed]

46. Zhou, C.; Gao, N.; Deng, Y.; Chu, W.; Rong, W.; Zhou, S. Factors affecting ultraviolet irradiation/hydrogen peroxide (UV/H2O2) degradation of mixed N-nitrosamines in water. *J. Hazard. Mater.* **2012**, *232*, 43–48. [CrossRef]

47. Graumans, M.H.F.; Hoeben, W.F.L.M.; Russel, F.G.M.; Scheepers, P.T.J. Oxidative degradation of cyclophosphamide using thermal plasma activation and UV/H2O2 treatment in tap water. *Environ. Res.* **2020**, *182*, 109046. [CrossRef]

48. De Filippis, P.; Scarsella, M.; Verdone, N. Peroxyformic acid formation: A kinetic study. *Ind. Eng. Chem. Res.* **2009**, *48*, 1372–1375. [CrossRef]

49. Cogliano, T.; Russo, V.; Turco, R.; Santacesaria, E.; Di Serio, M.; Salmi, T.; Tesser, R. Revealing the role of stabilizers in H_2O_2 for the peroxyformic acid synthesis and decomposition kinetics. *Chem. Eng. Sci.* **2022**, *251*, 117488. [CrossRef]

50. Salles, L.; Yves, P.J.; Thouvenot, R.; Minot, C.; Marie, B.J. Catalytic epoxidation by heteropolyoxoperoxo complexes: From novel precursors or catalysts to a mechanistic approach. *J. Mol. Catal. A Chem.* **1997**, *117*, 375–387. [CrossRef]

51. Bertleff, B.; Goebel, R.; Claußnitzer, J.; Korth, W.; Skiborowski, M.; Wasserscheid, P.; Jess, A.; Albert, J. Investigations on catalyst stability and product isolation in the extractive oxidative desulfurization of fuels using polyoxometalates and molecular oxygen. *ChemCatChem* **2018**, *10*, 4602–4609. [CrossRef]

52. Rajendran, A.; Fan, H.-X.; Cui, T.-Y.; Feng, J.; Li, W.-Y. Enrichment of polymeric WOx species in WOx@SnO$_2$ catalysts for ultra-deep oxidative desulfurization of liquid fuels. *Fuel* **2021**, *290*, 120036. [CrossRef]

53. Bertleff, B.; Haider, M.S.; Claußnitzer, J.; Korth, W.; Wasserscheid, P.; Jess, A.; Albert, J.J. Extractive catalytic oxidative denitrogenation of fuels and their promoting effect for desulfurization catalyzed by vanadium substituted heteropolyacids and molecular oxygen. *Energy Fuels* **2020**, *34*, 8099–8109. [CrossRef]

54. Otsuki, S.; Nonaka, T.; Takashima, N.; Qian, W.; Ishihara, A.; Imai, T.; Kabe, T. Oxidative Desulfurization of light gas oil and vacuum gas oil by oxidation and solvent extraction. *Energy Fuel* **2000**, *14*, 1232–1239. [CrossRef]

55. Farag, H. Selective adsorption of refractory sulfur species on active carbons and carbon based CoMo catalysts. *J. Colloid Interface Sci.* **2007**, *307*, 1–8. [CrossRef] [PubMed]

56. Lutterotti, L. MAUD Version 2.55. Available online: http://maud.radiographema.com (accessed on 15 May 2022).